

AN ABSTRACT OF THE THESIS OF

Joseph H. Haxel for the degree of Master of Science in Oceanography. Presented on February 1, 2002. Title: The Sediment Response of a Dissipative Beach to Variations in Wave Climate.

Abstract Approved:

Redacted for privacy

Robert A. Holman

Using wave and wind data from nearby buoys and gauges, real time kinematic global positioning system (RTK-GPS) and light detection and ranging (lidar) topographic survey data, and a robust video record, we have quantified the Large Scale Coastal Behavior (*LSCB*) of a dissipative end member beach in the Pacific Northwest. This study of Agate Beach from 1992 - 2001 reveals important observations of beach behavior on temporal and spatial scales that have received little attention in recent nearshore research. Similarly, the high-energy conditions characteristic of the Agate Beach study site define it as an dissipative end member that is not well understood.

In order to describe the variability of the system at spatial scales of hundreds of meters to kilometers and time scales of months to years, regression models for wave parameters and the beach sediment response were developed consisting of annually periodic functions superimposed upon long-term trends. The

amplitudes of the seasonal periodicity in significant wave heights ($A_{H_s} = 0.94 \text{ m} \pm 0.06$), dominant wave period ($A_{T_p} = 2.1 \text{ sec} \pm 0.1$), and mean wave direction ($A_{\theta} = 12.3^\circ \pm 2.0$) exhibit larger variability than the long-term trends observed within a year ($\beta_{H_s} = 6.7 \text{ cm/yr} \pm 2.6$, $\beta_{T_p} = 0.15 \text{ sec/yr} \pm 0.04$, $\beta_{\theta} = 3^\circ \text{ S/yr} \pm 1.0$).

Agreement between the long-term trends in wave statistics and morphology suggest a directly forced beach response. Assuming alongshore transport of sediment at Agate Beach is wave-driven, the long-term increase in significant wave heights (β_{H_s}) and change to a more southerly approach in wave direction (β_{θ}), coincident with the 1997-98 El Niño/ 1998-99 La Niña sequence, correlate with the increase in sediments along the beach ($\Delta V_b = 1.84 \times 10^5 \text{ m}^3$). Predictions of wave-driven alongshore transport estimate a net accretion at Agate Beach ($\psi_{net} = 2.73 \times 10^8 \text{ m}^3$) over the 9 year record length. In addition to the long-term increasing trend in sediment volume, a seasonally based fluctuation in sediments is observed ($A_{V_b} = 7.85 \times 10^4 \text{ m}^3 \pm 2.13 \times 10^4$). Video image analysis shows this increase in subaerial beach sediment volume at the northern end of the Newport littoral cell also coincides with the long-term offshore migration of the outer sand bar ($\beta_{OBx} = 11.0 \text{ m/yr} \pm 0.8$). This result also suggests accretion of sediments in a wider cross-shore region than observed in the survey record. Similar to the signature of beach volume variations, the cross-shore position of the outer sand bar also varies with season ($A_{OBx} = 114.9 \text{ m} \pm 4.2$). The seasonal migrations in the outer sand bar position displays much larger variations than the long-term behavior described by β_{OBx} .

Analysis of 27 topographic surveys resolves the cross-shore structure of the time varying beach surface. Using empirical orthogonal functions (EOF), 2 distinct eigen-modes of variance describe the seasonal patterns of sediment behavior at Agate Beach. The first mode describes 34% of the variance and is related to the summer growth of a dune field that is limited to elevations above MHW, $z = 1.076$ m. Analysis of concurrent wind field measurements shows this mode of variance is well correlated with aeolian processes. The second mode (21% of the variance) is wave-driven, and corresponds to the seasonal behavior of the beach surface below MHW. Observations show the MHW elevation serves as a transitional zone between dune related and wave-driven processes that affect the seasonal evolution of Agate Beach.

© Copyright by Joseph Henry Haxel
February 1, 2002
All Rights Reserved

The Sediment Response of a Dissipative Beach to Variations
in Wave Climate

by
Joseph H. Haxel

A THESIS

submitted to

Oregon State University

in partial fulfillment of
the requirements for the
degree of

Master of Science

Presented February 1, 2002
Commencement June 2002

Master of Science thesis of Joseph H. Haxel presented on February 1, 2002

APPROVED:


Redacted for privacy

Major Professor, representing Oceanography

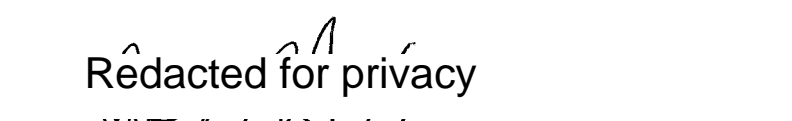

Redacted for privacy

Dean of College of Oceanic and Atmospheric Sciences

Redacted for privacy

Dean of Graduate School

I understand that my thesis will become part of the permanent collection of Oregon State University libraries. My signature below authorizes release of my thesis to any reader upon request.


Redacted for privacy

Joseph H. Haxel, Author

ACKNOWLEDGEMENTS

The waves, currents, sand, wind and generally the entire beach experience has been something I have loved since I was a young child. I have never lived far from the ocean. From countless hours spent in the water I developed a curiosity for the natural behavior of sand bars and changes in the beach that affected the quality of surf my friends and I rode at our home breaks. I would like to thank my advisor, Rob Holman, for giving me the opportunity, freedom and means to study a subject matter that is so close to my heart. Rob has given me the gift to know how to let the data tell the story. I would also like to thank him for his patience, encouragement, and understanding for my unorthodox approach to completing this degree in the last few months.

I would also like to thank John Stanley for writing codes that were 10X faster than the ones I developed, but not letting me know about them until I had taken 2 weeks to develop my own. His technical support, suggestions and jovial manner are something I will greatly miss. I would also like to thank members of the CIL, in particular: Chris, for never turning down a chance to do some field work (even in the snow/dark/rain) and countless hours of discussion and jokes; Nathaniel, for his development of the survey program, the first year of data, and help along the way; Hilary, for editorial comments and advice; Walt, for good stories and help with the argo and jet skis, and all the other people I have come in contact with throughout the Argus world for their time and insight.

Thanks to my family for their support and words of encouragement. Thank you Sammie for moving up to Oregon with me and volunteering to serve as the Coastal Imaging “Lab”, and Gus for just being “Goose”. And most importantly, thank you Jessica for believing in me and reminding me to always do what is good and right. And last but not least, thank you Mother Ocean for blessing us with your beauty.

This research was funded by the Office of Naval Research grant # N00014-96-10237.

TABLE OF CONTENTS

| | | |
|------------|---------------------------------------|----|
| Chapter 1: | INTRODUCTION..... | 1 |
| Chapter 2: | FIELD SITE AND DATA SOURCES..... | 5 |
| 2.1 | Field Site Description..... | 5 |
| 2.2 | Data Sources..... | 10 |
| 2.2.1 | Wave and Wind Climate Data..... | 10 |
| 2.2.2 | Topographic Data..... | 13 |
| 2.2.3 | Video Data..... | 19 |
| Chapter 3: | DATA ANALYSIS AND RESULTS..... | 23 |
| 3.1 | Introduction to Analysis Methods..... | 23 |
| 3.2 | Wave Climate Analysis..... | 23 |
| 3.3 | Wind Climate Analysis..... | 43 |
| 3.4 | Topographic Data Analysis..... | 44 |
| 3.4.1 | Gridding and Transformation..... | 44 |
| 3.4.2 | Beach Surface Change Analysis..... | 51 |
| 3.5 | Video Data Analysis..... | 68 |
| Chapter 4: | DISCUSSION..... | 75 |
| Chapter 5: | SUMMARY AND CONCLUSION..... | 81 |
| | REFERENCES..... | 84 |

LIST OF FIGURES

| <u>Figure</u> | <u>Page</u> |
|---------------|--|
| 2.1 | The location of Agate Beach and the NDBC coastal buoys along the Oregon coast.....6 |
| 2.2 | Aerial photograph of Agate Beach taken July 5, 2000 looking southward...7 |
| 2.3 | NDBC coastal buoys measure H_s , T_p and θ12 |
| 2.4 | The timeline of topographic surface data collected at Agate Beach from Argo (RTK-GPS) and lidar based surveys.....15 |
| 2.5 | The amphibious Argo and RTK-GPS measurement system.....16 |
| 2.6 | a) A snap shot of Agate Beach from the Argus video imaging system on top of Yaquina Head. b) A time exposure image from the same hour.....20 |
| 2.7 | A "daytimex" image composed of the daily average of pixel intensity calculated from the hourly 10 minute time exposures.....22 |
| 3.1 | Daily mean wave climate observations from the Newport (id# 46050) and Old Newport (id# 46040) offshore buoys.....25 |
| 3.2 | Time-lagged cross-correlation and extrapolation model fit for H_s from Newport and CRB buoy data.....26 |
| 3.3 | Time-lagged cross-correlation and extrapolation model fit for θ from Newport and CRB buoy data..... 27 |
| 3.4 | The combined records of Newport and extrapolated CRB daily mean observations of H_s (a), T_p (b), and θ (c) from buoy data..... 30 |
| 3.5 | Time-lagged auto correlation and annual model regression fit for H_s31 |
| 3.6 | Time-lagged auto-correlation and annual model regression fit for θ 32 |
| 3.7 | Monthly averaged ($\langle X(month, yr) \rangle$) and the repeated, 12 member set of monthly ensemble averaged annual ($\langle X_e(month) \rangle$) wave climate signals (a & c). (b & d), the long term linear trend fit to $\langle X(month, yr) \rangle - \langle X_e(month) \rangle$ 35 |

LIST OF FIGURES (continued)

| <u>Figure</u> | <u>Page</u> |
|---------------|--|
| 3.8 | $\langle H_{se}(month) \rangle$ plotted with the annual periodic regression model to show the intra-annual structure in the H_s variability.....36 |
| 3.9 | a) Daily estimates of Q_l from wave data. b) The low pass filtered Q_{lpf} time series of predicted alongshore sediment transport flux.....41 |
| 3.10 | The net annual time series of wave-driven alongshore sediment transport ψ_{annual}42 |
| 3.11 | Threshold filtered, monthly averaged wind speed and direction from an NDBC anemometer fixed 9.4 m above mean sea level on the south Yaquina Bay jetty..... 45 |
| 3.12 | RTK-GPS gridded data and interpolation errors from a topographic survey of Agate Beach on November 11, 2000..... 47 |
| 3.13 | The time-averaged beach surface elevation grid over the complete survey record length..... 49 |
| 3.14 | The transformation of the mean beach surface from Z to W space.....50 |
| 3.15 | Statistics of surface variability at Agate Beach over the survey record length..... 52 |
| 3.16 | The number of observations (N) at each grid node over the 27 survey record length..... 53 |
| 3.17 | The range in elevation at each grid node calculated by subtracting the minimum elevation from the maximum elevation observed throughout the survey time series..... 55 |
| 3.18 | The alongshore averaged statistics of the Agate Beach survey time series..... 56 |
| 3.19 | Statistics of Agate Beach as a function of surface elevation..... 58 |
| 3.20 | EOF analysis of the normalized survey record reveals two distinct modes of surface variability..... 61 |

LIST OF FIGURES (continued)

| <u>Figure</u> | <u>Page</u> |
|---------------|--|
| 3.21 | The dune mode EOF and monthly wind time series correlation..... 62 |
| 3.22 | The monthly mean alongshore wind velocity v_{wind} plotted against the dune mode amplitudes from the 1995-96 survey record..... 63 |
| 3.23 | a) A time exposure image of Agate Beach collected by the Argus station on top of Yaquina Head. The box indicates the study area covered by the topographic surveys. b) A cross-shore schematic diagram of the volumetric sediment calculation from equation 15..... 66 |
| 3.24 | The demeaned beach volume time series, V_b , calculated from all of the topographic surveys..... 67 |
| 3.25 | a) A rectified or plan view of the "daytimex" image from Figure 2.8 in local coordinates. b) The pixel intensity profile corresponding to each of the cross-shore transects shown in (a)..... 69 |
| 3.26 | The normalized timestacks composed of "daytimex" images from the 3 cross-shore profiles shown in Figure 3.24..... 71 |
| 3.27 | The "daytimex" timestack history of the cross-shore intensity profile at $y = 0$ m. The cross-shore position of the seaward edge of the outer sandbar ($ob_{x,0}$)..... 73 |
| 3.28 | The alongshore averaged, cross-shore position of the outer sand bar, OB_x , and the least squares multiple linear regression fit, OB_{xmod} , to the OB_x time series..... 74 |

LIST OF TABLES

| <u>Table</u> | | <u>Page</u> |
|--------------|--|-------------|
| 1 | Comparison of annual wave statistics, beach slopes and Iribarren #'s of 3 North American beaches..... | 9 |
| 2 | Contribution of NDBC Oregon coastal buoys for wave climate records at Agate Beach..... | 11 |
| 3 | Dates of Argo and Lidar topographic surveys of Agate Beach..... | 14 |
| 4 | Comparison of model coefficients for wave climate, beach sediment volume, and outer sand bar position..... | 76 |

LIST OF SYMBOLS

Symbol

| | |
|-----------------|--|
| β_x | long-term linear trend (equation 2) |
| β_{x0} | offset for regression fit (equation 2) |
| ΔV_{by} | the net increase in volume over the topographic survey time series |
| ε_x | unmodeled residuals (equation 2) |
| ϕ_x | phase of the seasonal cycle (equation 2) |
| γ_x | elevation skewness with respect to cross-shore position |
| γ_z | cross-shore skewness with respect to elevation |
| Γ_x | gain of the linear regression wave data extrapolation model (equation 3) |
| θ | wave angle |
| π | pi |
| ρ_{xy} | cross-correlation statistic |
| σ_x | standard deviation in elevation with respect to cross-shore position |
| σ_z | standard deviation in cross-shore position with respect to elevation |
| ξ | Iribarren number |
| Ψ_{annual} | net annual alongshore sediment volume transport from Q_l |
| Ψ_{net} | net total alongshore sediment volume transport from Q_l |
| ω | frequency of the seasonal cycle (equation 2) |

LIST OF SYMBOLS (continued)

Symbol

| | |
|------------|--|
| A_x | amplitude of the seasonal cycle (equation 2) |
| c | wave celerity |
| C_x | offset of the linear regression wave data extrapolation model (equation 3) |
| D | survey domain in Z space |
| D^* | survey domain D , transformed to W space |
| E | wave energy |
| E_{resx} | unmodeled residuals (equation 3) |
| g | gravitational acceleration constant |
| h | water depth |
| H_s | significant wave height |
| I | video image pixel intensity |
| I_l | alongshore immersed-weight transport rate |
| K | dimensionless constant |
| L_∞ | deep water wave length |
| $LSCB$ | Large Scale Coastal Behavior |
| n | ratio between wave group and phase velocity |
| N^* | effective degrees of freedom |
| $ob_{x,y}$ | cross-shore position of the outer sand bar with respect to alongshore location |
| OB_x | alongshore mean, cross-shore position of the outer sand bar |

LIST OF SYMBOLS (continued)

Symbol

| | |
|--------------------|---|
| OB_{xmod} | regression model of OB_x time series using equation 2 |
| P_l | alongshore component of wave power |
| Q_l | alongshore volume transport rate predicted from wave data |
| Q_{lpf} | low-pass filtered Q_l time series |
| Q_x | cross-shore sediment flux from survey data |
| Q_y | alongshore sediment flux from survey data |
| Q_{xy} | alongshore and cross-shore sediment flux from survey data |
| r_0 | radius of the circle fit to the time averaged 1 m elevation contour |
| r_{ext} | extended circle radius to fit entire survey domain |
| S | beach slope |
| S_{xy} | alongshore component of onshore radiation stress |
| T_p | dominant wave period |
| $U \text{ and } V$ | video image pixel coordinates |
| v_{tg} | critical wind velocity threshold to transport Agate Beach sands |
| v_{wind} | monthly mean alongshore wind velocity from threshold limited record |
| V_b | observed volume of sediment in survey region |
| V_{model} | regression model of V_b time series using equation 2 |
| W | complex space where alongshore curvature from Z space is removed |

LIST OF SYMBOLS (continued)

Symbol

| | |
|--|---|
| x | offshore increasing, cross-shore direction in local coordinates |
| x' | offshore increasing, cross-shore direction in transformed W space |
| $\langle X_e(\text{month}) \rangle$ | 12 member set of ensemble-averaged monthly statistics |
| $\langle X(\text{month}, \text{yr}) \rangle$ | monthly averaged statistics |
| y | alongshore direction in local coordinates |
| y' | alongshore direction in transformed W space |
| z | elevation with respect to NGVD29 |
| Z | complex space defined in local x and y coordinates |

THE SEDIMENT RESPONSE OF A DISSIPATIVE BEACH TO VARIATIONS IN WAVE CLIMATE

Chapter 1 INTRODUCTION

As sea level rises, the threat of coastal erosion has become an increasing concern to beachfront developers, property owners and coastal planners. Beach erosion events strip large volumes of sand from the beach face, and transport it offshore and alongshore on varying spatial scales. While one area of a beach is hit hard by the onset of storm waves and loses the majority of sand on its beach face, another region of the beach, sometimes only a few kilometers away may experience little loss. Alternatively, during calmer months, certain areas of the beach may experience larger amounts of accretion. These fluctuations in the volume of sand along a beach affect its ability to serve as a dissipative buffer in protecting valuable property from the attack of high-energy storm waves. An understanding of the behavior of beaches on a variety of temporal and spatial scales is required to make accurate model predictions of the sediment response to both short and long-term variations in forcing.

Beach erosion events are episodic in nature and well correlated with the arrival of high-energy storms at the coastline. Modern nearshore science has focused on processes involving short-term beach variability at time scales of seconds to weeks and length scales of centimeters to hundreds of meters. Observations of short-term beach and sand bar behavior are based on short, intense

field experiments (Sallenger et al., 1985; Gallagher et al., 1998, Plant and Holman, in review). These types of studies of beach and sand bar behavior have improved the knowledge base as well as the performance of process based models in describing the short-term morphologic evolution of beaches.

Despite the improvements in short-term (seconds to weeks) process models of sediment transport and morphologic change, when integrated through time, these models produce results that are generally thought to be unrealistic (Stive et al., 1995, De Vriend, 1997). As process based models are stepped through longer time intervals, non-linear interactions between the morphology and fluids are often not accounted for and may create instabilities within the long-term evolution of the system.

In addition to the episodic erosion of beaches caused by single storm wave events, longer-term seasonal variability in beach and sand bar behavior may be introduced by the succession of storm arrivals during the winter (van Enckevort, 2001). Monthly changes in morphology and beach profiles have been correlated with seasonal changes in wave climate (Winant et al., 1975; Aubrey, 1979 & 1983). As wave heights increase, winter profiles are defined by a shallow beach slope and intertidal bar. Conversely, as wave heights subside, summer profiles are marked by a steeper beach with the bar welded to the shoreline. The cross-shore position of the offshore sand bars is an important indicator for seasonal beach profile changes brought on by variations in the wave climate. Birkemeier (1984) also linked the onshore/ offshore migration of offshore sand bars to seasonal changes in forcing.

The seasonal changes in cross-shore profile and offshore/ onshore sand bar migration indicate a seasonal cross-shore sediment transport pattern. Estimates of the seasonal cross-shore flux of sediments along beaches have hardly been quantified.

The variability of beaches and sand bars on longer temporal and spatial scales, termed Large Scale Coastal Behavior (*LSCB*), is not well understood. The behavior of beaches on the scale of years to decades and kilometers has received less attention than process based studies. The few long-term data sets that are available reveal unexpected behavior (Plant, et al., 1999, Wijnberg and Terwindt, 1995, Ruessink and Terwindt, 2000). Along several coastlines, a nearly decadal cycle of bar generation near the shoreline, migration offshore, and subsequent bar degeneration offshore has been documented. In these studies, this cycle has not been related to similar variations in the wave climate. Instead, the behavior seems to be linked to non-linear feedback interactions between the bars themselves (Ruessink and Terwindt, 2000).

The variability of beaches at *LSCB* scales is generally attributed to one of direct forcing, nonlinearities in direct forcing, nonlinear feedback mechanisms or some combination of these (Holman and Lippman, 1998). The first two of these possible mechanisms for beach variability are related to changes in the forcing (winds, waves, currents, etc.) and are therefore termed a forced response. For example, the seasonal beach profiles related to winter and summer wave climate conditions outlined above can be called a forced response. The third form is known

as free behavior since it is the result of instabilities caused by feedback between the morphology and fluids within the system. The yearly to decadal birth, offshore migration and degeneration cycle of the sand bars discussed earlier are most likely manifestations of free behavior.

In this study, wave climate variability is correlated to the forced sediment response of a beach system in the Pacific Northwest. Large changes in wave direction coupled with increased wave heights along the Pacific Northwest coast combined to produce northward transport of beach sediments. A predictive equation for alongshore sediment transport based on wave driven currents is compared to field data. Similarly, cross-shore and alongshore sediment fluxes are quantified using estimates made from topographic beach survey data.

The high-energy nature, low slopes and rugged conditions of Pacific Northwest beaches makes them dissipative end members that have received little attention in nearshore research. Using buoy and wind data, topographic survey measurements and video morphologic analyses, this study quantifies the long-term and annual behavior of Agate Beach in response to long-term and annual variations in wind and wave forcing. Patterns of topographic beach surface variability document where, when, and how the beach surface responds to seasonal changes in the wind and wave climates, as well as long-term variations brought on by El Niño and La Niña ocean conditions.

Chapter 2 FIELD SITE AND DATA SOURCES

2.1 Field Site Description

The Oregon coastline is divided into a series of sandy beaches bounded by basaltic headlands. The continuous stretches of beach between headlands are known as littoral cells, and are believed to be closed systems with respect to the volumes of beach sediments they contain (Komar, 1997). Agate Beach is located at the northern terminus of the Newport littoral cell on the central Oregon coast (Figure 2.1). The Newport littoral cell extends along 42 km of coastline, bounded by Yaquina Head to the north, and Cape Perpetua to the south. Two westward extending rock jetties stabilize the entrance to Yaquina Bay and further divide the Newport littoral cell into sub-cells. The 5 km long northern sub-cell runs from the north Yaquina Bay jetty up to Yaquina Head (Figure 2.2). Agate Beach is the 2.5 km stretch of sand within the sub-cell, extending from the southern face of Yaquina Head to the rocks at the northern end of Nye Beach.

Alongshore curvature of Agate Beach forces directional adjustments of breaking waves due to refractive processes. Another important aspect of the study site is the shadowing effect of Yaquina Head on the northern section of Agate Beach. Swells approaching from a northwesterly direction are partially blocked or refracted by the large headland that extends 1.5 km from shore. Therefore, the largest portion of wave energy from northwest swells impacts the southern section

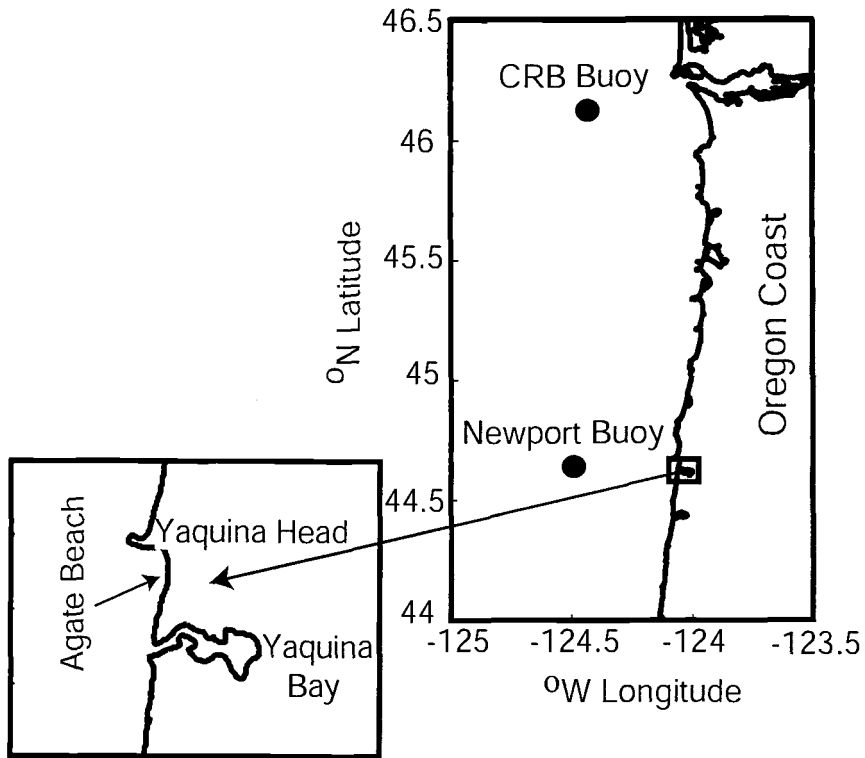


Figure 2.1 Agate Beach is located at the northern end of the Newport littoral cell on the central Oregon coast. The location of the NDBC coastal wave buoys used in this study are shown as dots. The geographic location of Agate Beach as the northern terminus of a littoral cell makes it an ideal site for the study of alongshore sediment transport.

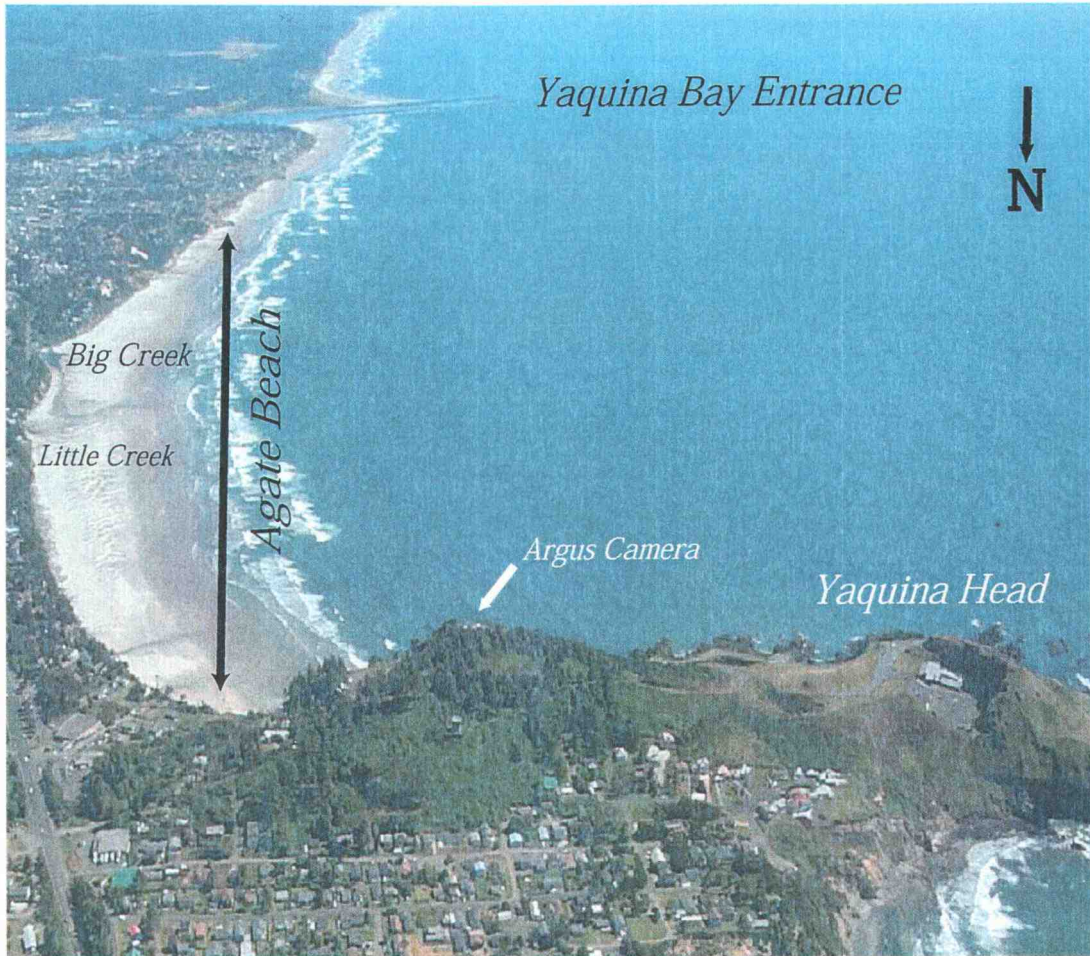


Figure 2.2 Aerial photograph of Agate Beach taken July 5, 2000 looking southward. Note the alongshore curvature of the beach, as well as the northward bend in Big Creek.

of Agate Beach. Aside from its slight alongshore curvature, Agate Beach generally faces west allowing full exposure to most of the high-energy storms and swells generated in the North Pacific Ocean. A small offshore reef in 12 m water depth roughly 1.5 km from shore offers little protection from the continuous attack of winter storms.

The sediments at Agate Beach are medium-grained sand, composed mostly of quartz and feldspar with median grain diameters around 0.2 mm (Ruggiero, 1997). The beach slopes gradually $O(0.01)$ and is exposed to large semi-diurnal tides ranging from 2-3 m. At lower tidal elevations there may be up to 600 m of exposed, subaerial, cross-shore beach surface. Because of its gradual slope, during large winter storms the surf zone may span up to 1 km as breaking waves dissipate their energy across the offshore sand bars.

When compared with the incident wave energy impacting other North American beaches, Agate Beach stands out as a high-energy end member (Table 1). Comparing the Iribarren numbers (ξ)

$$\xi = \frac{S}{\left(\frac{H_s}{L_\infty}\right)^{1/2}} \quad (1a)$$

$$L_\infty = \frac{gT_p^2}{2\pi} \quad (1b)$$

of three representative beaches from the U.S. coastline further reveals the dissipative nature of Agate Beach defined within the morphologic framework of Wright and Short (1983). The large waves and low sloping characteristics of Agate

Beach place it well within Wright and Short's (1983) dissipative end member criterion ($\xi < 0.3$).

Table 1 Comparison of annual wave statistics, beach slopes and Iribarren numbers of 3 representative North American beaches (*statistics from this study; †from Guza and Thornton,1981; ‡ from Birkemeier,1985)

| Site | H_s (m) | T_p (sec) | S | ξ |
|----------------------|-----------|-------------|------|-------|
| Agate Beach, OR* | 2.33 | 10.6 | 0.01 | 0.09 |
| Torrey Pines, CA† | 1.10 | 12 | 0.02 | 0.29 |
| Duck, NC‡ | 0.89 | 8.8 | 0.05 | 0.58 |

During a normal year, the net alongshore transport of sediment from wave-driven currents within the Oregon littoral cells is expected to be zero (Komar, 1998a). Winter waves arriving from the southwest generate northward alongshore flows that tend to deposit sediment on Agate Beach as the flow encounters the headland. Conversely, summer waves coming from the northwest drive southward alongshore flows that strip sediments away from Agate Beach and deposit them further south within the littoral sub-cell. During El Niño years, the winter pattern is strengthened by not only a higher frequency of storm wave occurrences, but also larger storm waves arriving from a southerly direction (Komar, 1986). Therefore,

during El Niño events, Agate Beach experiences an accumulation of sediment resulting from strong northward flows.

Oregon coast weather has a prominent effect on the seasonal evolution of Agate Beach. During winter months, an onslaught of intense southerly winds and driving rains batter the coastline, while the summer is characterized by drier, warmer air temperatures and northwesterly winds (Komar, 1997). One result of this seasonal pattern is variation in the impact of two creeks (Big Creek and Little Creek; Figure 2.2) that cross the beach. During periods of intense rainfall in the winter, these creeks cut down and wash upper beach sediments into the inner surf and swash zone creating offshore deltas (Ruggiero, 1997). Conversely, in summer the precipitation is at a minimum, and the upper beach sediments dry out from lack of rain and swash infiltration. Strong northwesterly summer winds then generate a seasonal dune field in the backshore (Figure 2.2). At their seasonal peak in September, some dunes reach heights of nearly 2 m and the field may encompass 50,000 m². Later in the fall when the wave energy increases, the sand in these dune fields is recovered by the swash and returned offshore.

2.2 Data Sources

2.2.1 Wave and Wind Climate Data

Wave climate data has been collected by NOAA's National Data Buoy Center (NDBC) in Oregon's offshore coastal waters near Agate Beach since 1987.

The wave record used in this study is compiled from observations collected by three coastal buoys (Table 2). The Newport buoy is located ~30 km WSW of Agate Beach while the Columbia River Bar (CRB) buoy is located ~170 km NW of the study site (Figure 2.1). The old Newport buoy was located ~2 km north of the present day Newport buoy position, making any measurement differences negligible for the purpose of this study.

Table 2 Contribution of NDBC Oregon coastal buoys for wave climate records at Agate Beach

| Old Newport (#46040) | Newport (#46050) | CRB (#46029) |
|-----------------------------|-------------------------|--|
| 05/28/87 - 11/11/91 | 11/12/91 - 08/31/00 | Filling gaps in Newport record 11/12/91-08/31/00 |

The NDBC buoys deployed in Oregon's offshore coastal waters provide measurements of significant wave heights (H_s), peak spectral periods (T_p), and mean wave directions (θ) (Figure 2.3). The buoys are moored in 130 m water depths, roughly 15 km from shore. Each of the wave parameters is sampled for 20 minutes at the start of every hour throughout the day. Significant wave height (H_s) is recorded as the average of the upper 1/3 of the measured waves within the sampling period (<http://www.NDBC.noaa.gov/>). Dominant period (T_p) is measured as the peak in the wave energy spectrum, and θ is evaluated as the mean wave

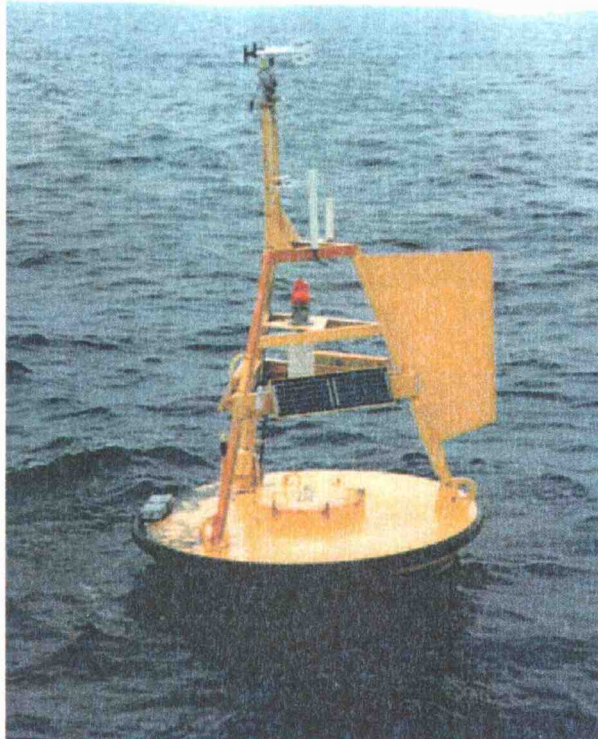


Figure 2.3 The NDBC offshore buoys measure H_S , T_P and θ for 20 minute intervals every hour. The Newport and CRB buoys are moored in 130 m water depths in Oregon's offshore coastal waters.

direction associated with the dominant spectral peak. This information provides a description of the wave climate at Agate Beach over the last 13 years. A NOAA based tidal gauge (#9435380) in Yaquina Bay also provides tide level observations referenced to NGVD29 for the Agate Beach area.

Concurrent wind measurements from an NDBC gauge located on the south Yaquina Bay jetty provide a description of the wind forcing at Agate Beach. The NDBC anemometer is mounted on a tower 9.4 m above mean sea level roughly 3 km south of the study site. Values for wind velocity and wind direction are calculated and recorded from 2 minute averaging intervals at the top of every hour.

2.2.2 Topographic Data

The recent advances in survey technology based on global positioning systems (GPS) have allowed for the dense and accurate coverage of large spatial areas (Morton et al., 1993; Dail et al., 2000; Plant and Holman, in review). In the past, covering these large areas of beach with high sampling density over short time intervals was unimaginable using traditional optical surveying methods. In addition to the advantages in surveying speed, real time kinematic global positioning system (RTK-GPS) based techniques provide more accurate position estimates than traditional optical tracking techniques (Plant and Holman, in review).

Two RTK-GPS beach survey series were carried out collecting topographic data of Agate Beach in 1995-96 and 2000-01 (Table 3 and Figure 2.4). These

Table 3 Dates of Argo and Lidar topographic surveys of Agate Beach

| RTK-GPS survey series #1 1995 - 1996 | Lidar surveys 1997 - 1998 | RTK-GPS survey series #2 2000 - 2001 |
|---|--------------------------------------|---|
| 06-14-95 | 10-17-97 | 05-25-00 |
| 06-28-95 | 04-24-98 | 06-21-00 |
| 07-12-95 | | 07-19-00 |
| 07-27-95 | | 08-29-00 |
| 08-10-95 | | 09-26-00 |
| 08-25-95 | | 11-13-00 |
| 09-08-95 | | 12-11-00 |
| 09-29-95 | | 01-09-01 |
| 10-27-95 | | 02-05-01 |
| 12-09-95 | | |
| 01-05-96 | | |
| 02-17-96 | | |
| 03-16-96 | | |
| 04-20-96 | | |
| 05-18-96 | | |
| 06-15-96 | | |

surveys were undertaken using an RTK-GPS mounted on a six wheel, amphibious, all terrain vehicle known as the Argo (Figure 2.5), enabling quick and accurate elevation measurements of the subaerial beach surface during low tide intervals. By sampling during spring low tide conditions (often in the dark), these surveys cover the greatest possible cross-shore extent of subaerial beach surface during each month. Each survey covers roughly 400 m in the cross-shore and 2.5 km in the alongshore. Sampling at 5 Hz, the current data collection system is capable of making accurate measurements at vehicle speeds up to 10 m/s. The beach surveys

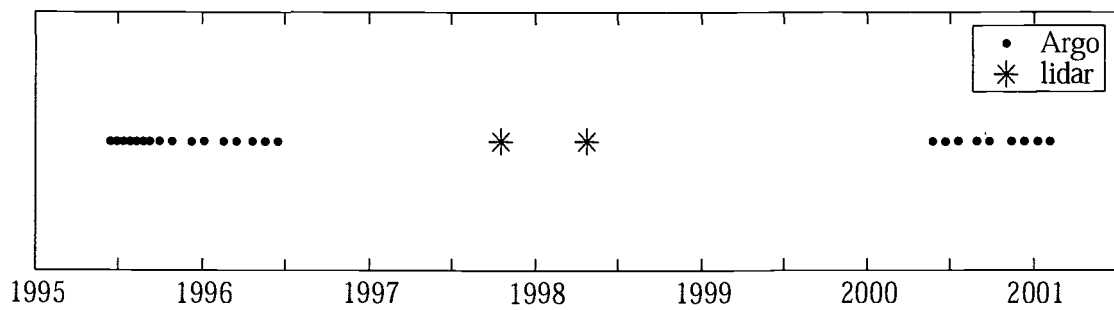


Figure 2.4 The time history of topographic surface data collected at Agate Beach from Argo (RTK-GPS) and lidar based surveys.

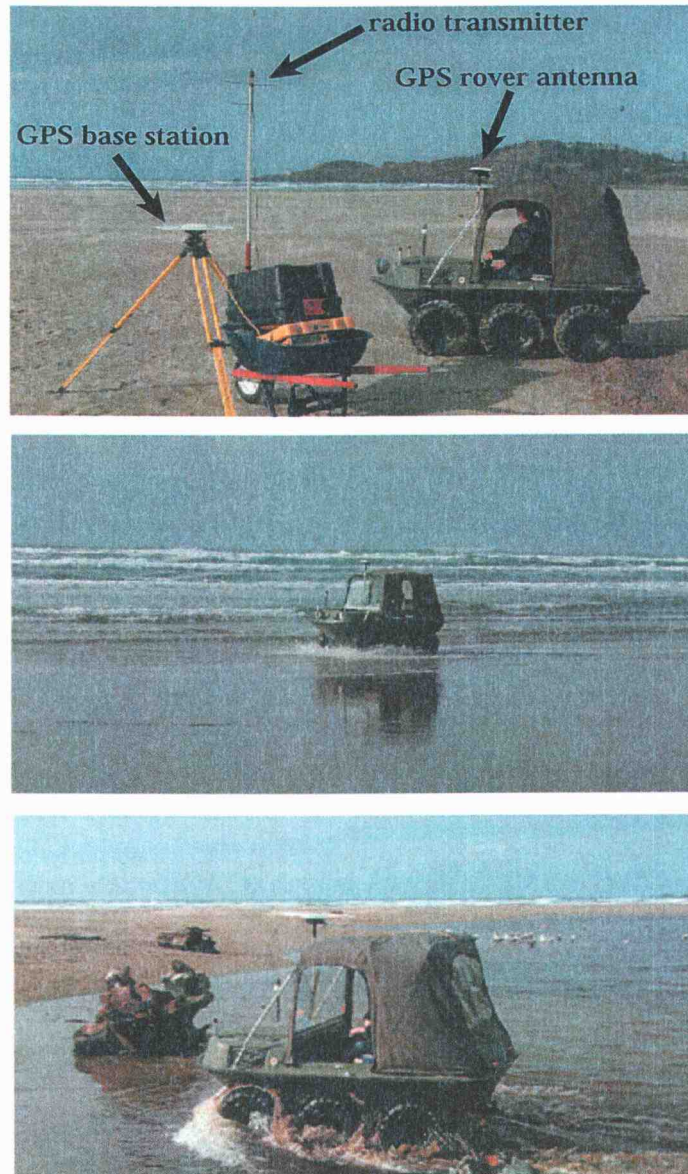


Figure 2.5 The RTK-GPS collection system. The top panel shows the base station unit and radio transmitter antenna along with the rover GPS unit mounted on the Argo. Topographic estimates can be collected at vehicle speeds up to 10 m/s. The amphibious nature of the Argo makes it possible to measure the beach surface through creek beds and incoming swash.

from series #2 are composed of more than 40,000 elevation measurements collected in time intervals of 2.5 hours.

The RTK-GPS collection system employed in this study is similar to that used by Plant and Holman (in review). The survey grade GPS equipment consists of a base station with a known position, a GPS rover unit mounted on the Argo (Figure 2.5), and a high powered radio transmitter and receiver. The base station and rover units (Trimble 7400) collect simultaneous range measurements from a common group of satellites. The base station compares a measured position with its known reference position and sends an error correction to the rover unit via the high-power radio transmitter. The real time kinematic correction supplied by the base station allows for rover estimates with errors $O(3\text{cm})$ in the horizontal and $O(5\text{cm})$ in the vertical. The position measurements made by the RTK-GPS system are logged on a Fieldworks Inc. computer running Trimble's Hypack software. To correct for antenna height, the elevation of the RTK-GPS rover antenna mounted on the Argo is measured during each survey and subtracted from all beach surface observations.

In October 1997 and April 1998 a collaborative effort between the National Aeronautic and Space Administration (NASA), the National Oceanic and Atmospheric Administration (NOAA), and the United States Geological Survey (USGS) collected topographic data along the California, Oregon, and Washington coasts in order to capture changes resulting from a strong El Niño event. Using lidar (light detection and ranging) technology, airborne surveys made surface

elevation measurements of the Oregon coastline, including the study area at Agate Beach. Lidar is a remote sensing, laser-based technology capable of collecting vast amounts of densely sampled topographic data in short time intervals (Sallenger et al., 1999). The system collects 3,000 to 5,000 surface elevation shots per second, yielding roughly 600,000 survey points within the Agate Beach study area for each survey date. The estimated vertical accuracy of the system is 15 cm (Sallenger, et al., in review). This data, supplied by the NOAA Coastal Services Center, supplements the temporal gap in the survey record between the 1996 and 2001 RTK-GPS survey series. By combining the RTK-GPS and lidar data, this study focuses on topographic changes across 27 surveys spanning 6 years at Agate Beach.

The topographic data are transformed with a rotation and translation into the local right hand coordinate system common to the video data with x increasing offshore. During each survey operation, local control points are collected and their position is used to calculate the transformation of all the survey observations into the local coordinate system. All elevations reported are referenced to the National Geodetic Vertical Datum (1929). Due to the low sloping nature of Agate Beach, and small footprint of the Argo, elevation errors resulting from the Argo tilt were small (within the RTK-GPS instrument error) and therefore neglected (Plant and Holman, in review).

2.2.3 Video Data

The powerful waves, extensive surf zone, and strong currents associated with the dissipative conditions at Agate Beach make it difficult to collect continuous, in situ measurements of geophysical variables (i.e. currents, waves, subaqueous profiles). An Argus video imaging system was installed in 1992 by the Coastal Imaging Lab on top of Yaquina Head to study nearshore processes (Figure 2.2). The accumulated video data set provides ideal temporal and spatial coverage of offshore sand bar locations. Remote sensing techniques based on these video images are used to characterize the sediment transport patterns and the morphologic evolution of the offshore sandbars along Agate Beach.

A snap shot of Agate Beach (Figure 2.6a) from the video imaging system on top of Yaquina Head captures breaking waves as intermittent patches of white foam. A time exposure image with the same field of view is created every hour. Time exposure images are sampled at 1 Hz and are computed as the time-averaged intensity at each pixel over a 10 minute period. These images resolve the spatial location of preferential wave breaking indicated by smoothed, bright bands of pixel intensity (Figure 2.6b). The bright bands of intensity correspond to the locations of shallow bathymetric features such as sandbars and the shoreline (Holman and Lippmann, 1987). Time exposure images of Agate Beach have been collected hourly since 1992. To reduce the data set for this analysis, we use "daytimex" images composed of the mean pixel intensity from each time exposure image within a day (Konicki and Holman, 2000). These images have the advantage of

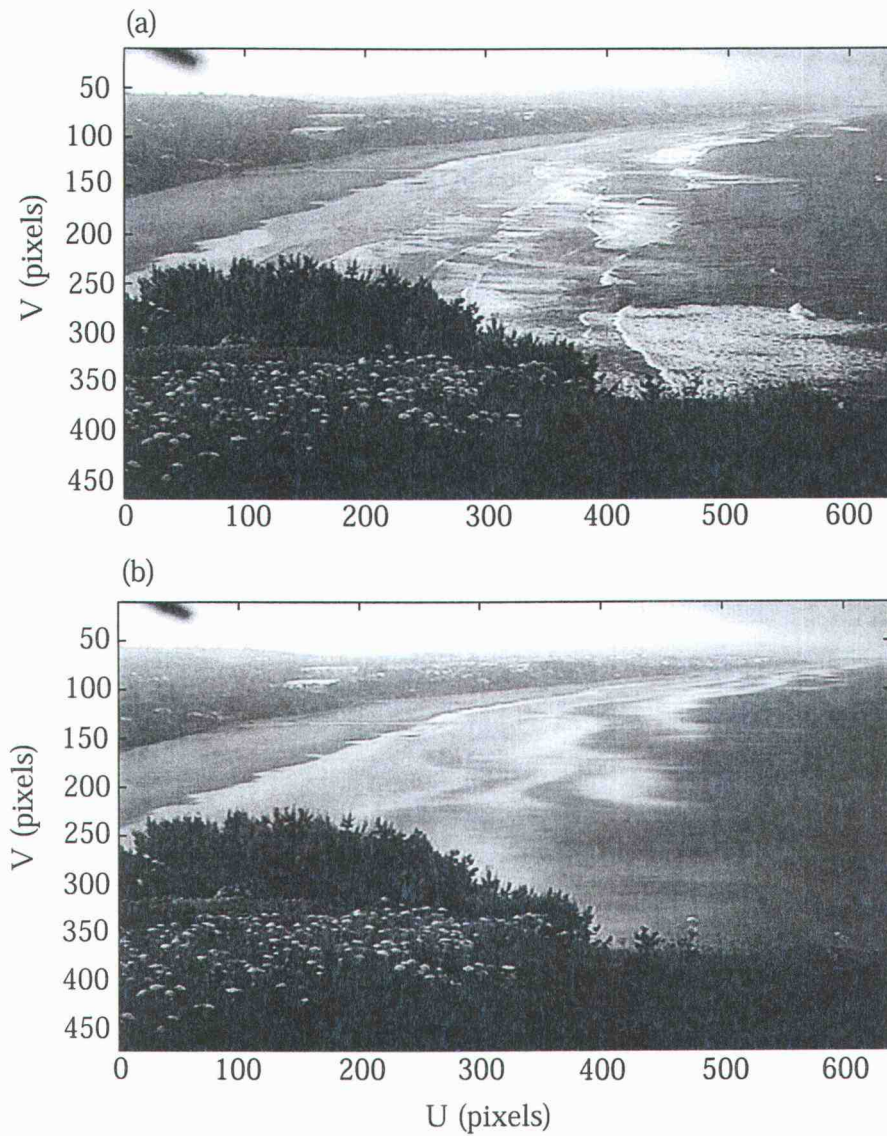


Figure 2.6 a) A snap shot of Agate Beach from the Argus video imaging system on top of Yaquina Head. b) A time exposure image from the same hour. Time exposure images consist of the time averaged pixel intensity over a 10 minute period sampled at 1 Hz. Note the continuous white bands of foam indicating the position of the offshore sand bars.

merging image features that were only visible during certain tidal conditions. Because they are composed of a continuum of images spanning the daily tidal cycles, these "daytimex" images capture the shoreline at high tide as well as sandbars that are only revealed through wave breaking during lower tidal conditions (Figure 2.7). A total of 3128 "daytimex" images from June 5, 1992 through March 3, 2001 provide a time series for daily estimates of the outer sand bar location.

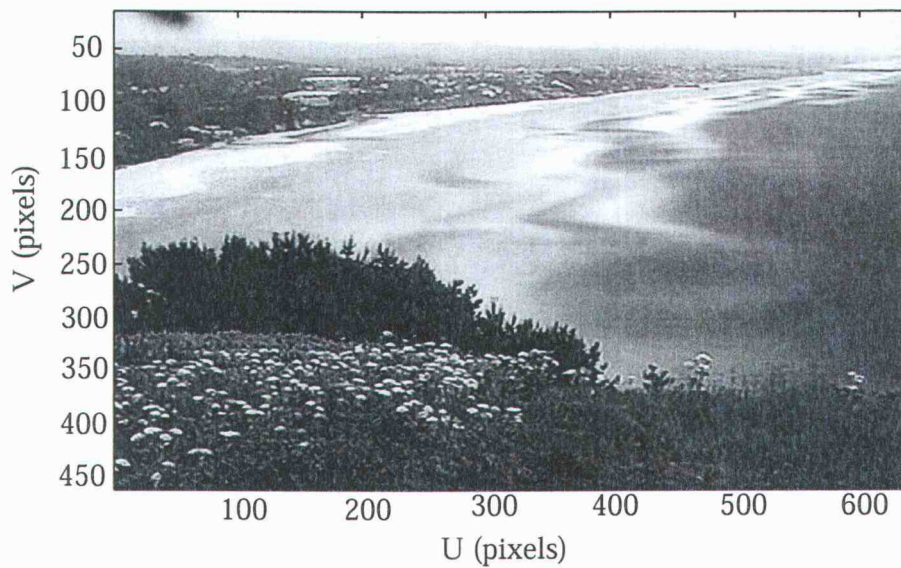


Figure 2.7 A "daytimex" image composed of the daily average of pixel intensity calculated from the hourly 10 minute time exposures. These images have the advantage of spanning the tidal conditions and therefore give a representative estimate of wave breaking patterns throughout the tidal cycles.

Chapter 3 DATA ANALYSIS AND RESULTS

3.1 Introduction to Analysis Methods

To uncover the relationship between the temporal and spatial sediment response of Agate Beach to the changes in wave and wind climates, we compare regression model coefficients produced from variations in H_s , T_p , θ , the beach volume measured from topography (V_b), and the cross-shore position of the outer sand bar (OB_x). Each of these parameters is modeled as the sum of a periodic annual signal superimposed upon a long-term trend (2).

$$X(t) = A_x \cos(\omega t + \phi_x) + \beta_x t + \beta_{x0} + \varepsilon_x \quad (2)$$

In equation 2, X represents the time series of the modeled variable. The $A_x \cos(\omega t + \phi_x)$ term represents the periodic annual signal, while $\beta_x t$ describes the longer-term behavior of the time series. β_{x0} is an offset, and ε_x indicates the unmodeled residual variability within the record. Using the information obtained from regression model fits to these data, we construct a useful quantification of the seasonal and *LSCB* of the Agate Beach system.

3.2 Wave Climate Analysis

Breaking waves in the nearshore produce the turbulent energy required to suspend beach sediments within the water column, which are then advected in the

cross-shore and alongshore directions by currents and other low frequency flows. The magnitudes and directions of these low frequency flows are largely governed by the directions and intensities of the incident wave energy (Thornton and Guza, 1986; Komar and Oltman-Shay, 1990). In this study we focus on the incident wave energy band as a means to characterize the general wave climate associated with nearshore sediment transport along Agate Beach.

Daily mean values for H_s , T_p , and θ are calculated from the hourly measurements made by the NDBC buoys described in section 2.2.1. The wave directions are adjusted to a local right-hand coordinate system (positive x increasing offshore) associated with 0° normal incidence at the center of alongshore curvature of Agate Beach. Within the local coordinate system, negative incident angles correspond to waves approaching from the north. The daily mean values for the combined Newport buoy stations are shown in Figure 3.1. Unfortunately, there are significant gaps within the Newport record, particularly with regard to wave direction.

To produce a longer, more continuous time series of wave statistics, the CRB buoy data is extrapolated to the Newport region by a linear model.

$$X_{(Newp)}(t) = \Gamma_X X_{(CRB)}(t) + C_X \quad (3)$$

X represents the wave climate variable. Γ_X and C_X represent the gain and offset of the least squares regression model. The regression analysis reveals an offset in H_s and θ between the CRB and Newport records (Figure 3.2 & 3.3). The extrapolation

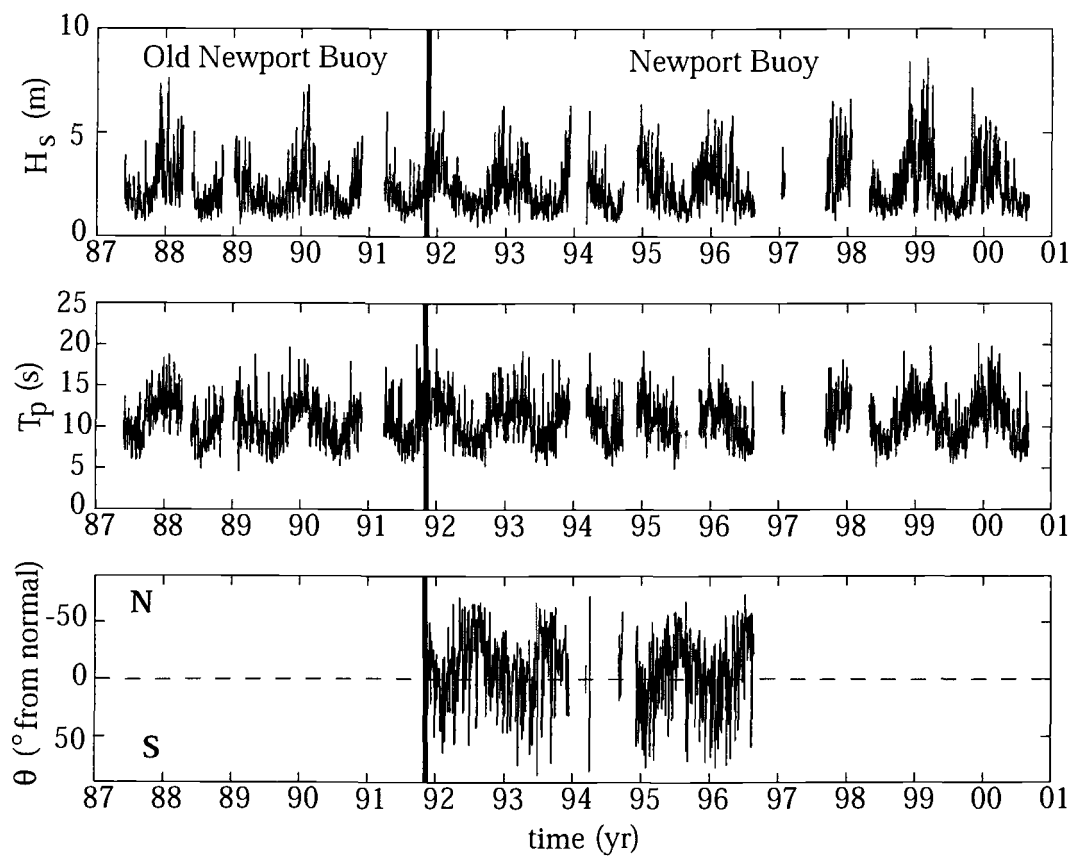


Figure 3.1 Daily mean wave climate observations from the Newport (id# 46050) and Old Newport (id# 46040) offshore buoys. Notice the annual cycle in each parameter as well as some of the large gaps in the record, particularly with respect to θ .

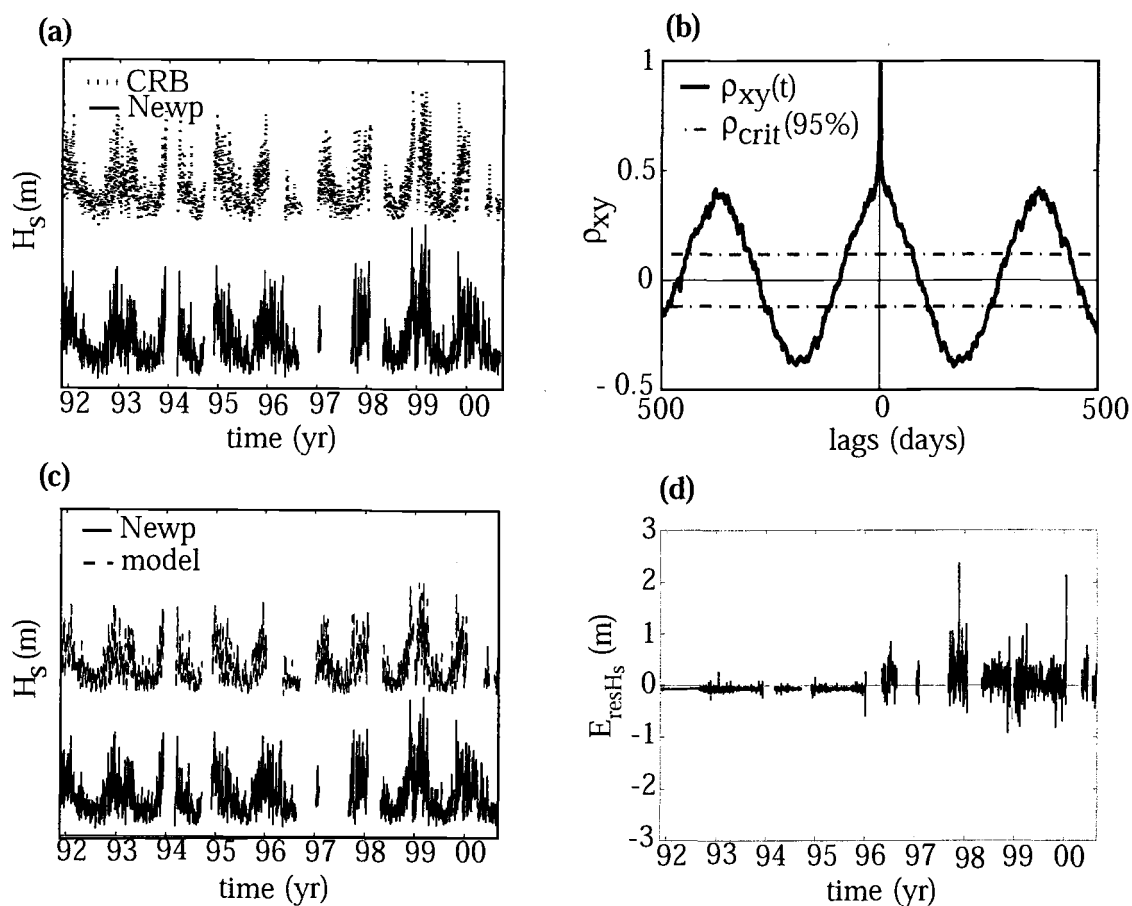


Figure 3.2 Time-lagged cross-correlation and extrapolation model fit for H_S from Newport and CRB buoy data. **a)** The Newport and CRB daily mean H_S observations during times the records overlap. **b)** Time-lagged cross-correlation between the CRB and Newport records. **c)** The least squares linear model used to extrapolate the CRB H_S values to the Newport area where gaps in the record exist. **d)** The residuals (E_{resH_S}), calculated by subtracting the model results from the Newport data.

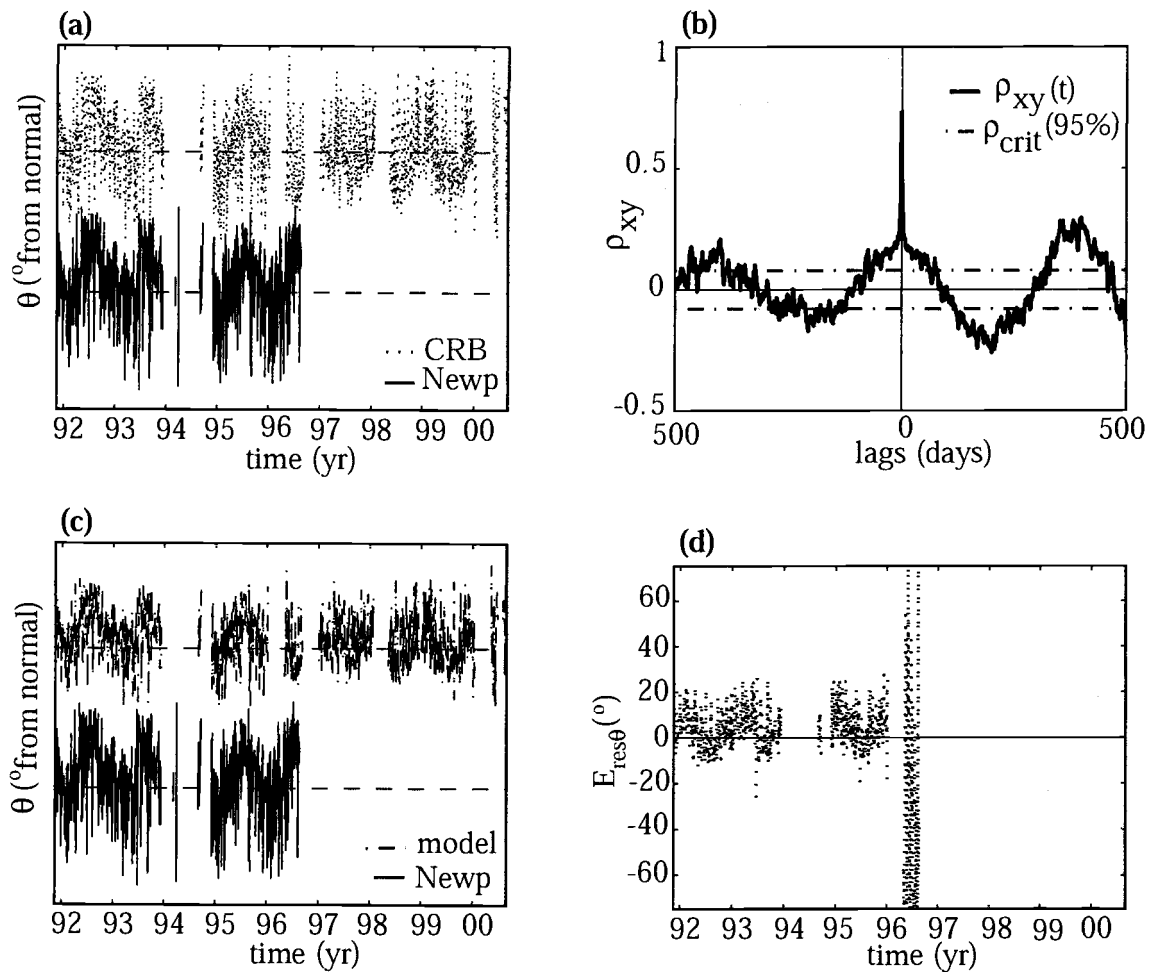


Figure 3.3 Time-lagged cross-correlation and extrapolation model fit for θ from Newport and CRB buoy data. **a)** Overlapping daily mean observations for θ from the CRB and Newport buoys. **b)** Time lagged cross-correlation between the records. **c)** Linear least squares model fit used to extrapolate the CRB θ values to the Newport region where gaps in the record exist. **d)** The residuals ($E_{res\theta}$), calculated by subtracting the regression model from Newport data.

model for H_s has a gain $\Gamma_{H_s} = 1.0$ and offset $C_{H_s} = 0.05$ m, revealing significant wave heights from the Newport buoy are on average 5 cm higher than those at the CRB location. Similarly, the extrapolation model for θ has a gain $\Gamma_{\theta} = 0.74$ and offset $C_{\theta} = -6^\circ$ revealing wave directions from the Newport buoy are offset by 6° north from waves arriving at the CRB buoy location. The drop in Γ_{θ} indicates the CRB wave angles move through larger ranges than wave directions at the Newport buoy.

A time lagged cross-correlation analysis between the different records of H_s and θ is used to correct for any temporal lag in storm wave arrival due to the latitudinal distance between the CRB and Newport buoys (Figures 3.2 & 3.3). Since observations of wave directions begin nearly 5 years after measurements of wave energy, this cross-correlation, and any other subsequent analysis that employs wave direction are based on a truncated portion of the entire record beginning in 1992. This analysis reveals a dominant and significant peak at zero lag for each parameter ($\rho_{xy, H_s}(0) = 0.99$ and $\rho_{xy, \theta}(0) = 0.79$), indicating a strong correlation between the records at the 95% level. The peak at zero lag suggests that waves arrive at the Newport and CRB buoys on the same day. A lag in storm wave arrival between the buoys on the scale of hours may exist, but by using a daily mean statistic, this temporal lag is effectively smoothed over.

The residuals (E_{resx}) left by subtracting the model hindcast from Newport wave height data show agreement between the model estimates and observations in

the early part of the record, followed by decreasing accuracy in the latter part of the record. The abrupt fall in the accuracy of the extrapolation models (~1996-97) is likely caused by inconsistencies in the instruments used to measure the wave parameters. Around the time of these suspicious changes in the data, the buoy hulls and instrument packages used to measure and record the wave climate observations at each buoy location were altered (<http://www.NDBC.noaa.gov/>).

Figure 3.4 shows the resulting, merged daily mean time series for each of the wave statistics at Agate Beach. The decrease in variance of the merged record for θ after 1997 is also observed in the CRB record (Figure 3.3), and is therefore not attributed to an error in our analysis. While these data provide a detailed record of the wave climate over the last 13 years, the time series is too short for good frequency resolution with traditional spectral techniques. As a result, a time lagged auto correlation analysis is used to isolate the dominant periodic signals within the H_s and θ records (Figures 3.5, 3.6). The auto correlation analysis of the raw time series for H_s reveals a mean in the time difference between peaks in the lags at 365 days at the 95% confidence level (Figure 3.5).

Confidence intervals for all variables in this analysis are estimated using the effective degrees of freedom (N^*) calculated from the artificial skill method of Chelton (1983). Although the H_s time series has a longer record length than θ , its confidence interval is larger due to the large decrease in N^* ($N^*_{H_s} = 75$ and $N^*_\theta = 678$). As Figures 3.5a & 3.6a show, the H_s record contains less high frequency

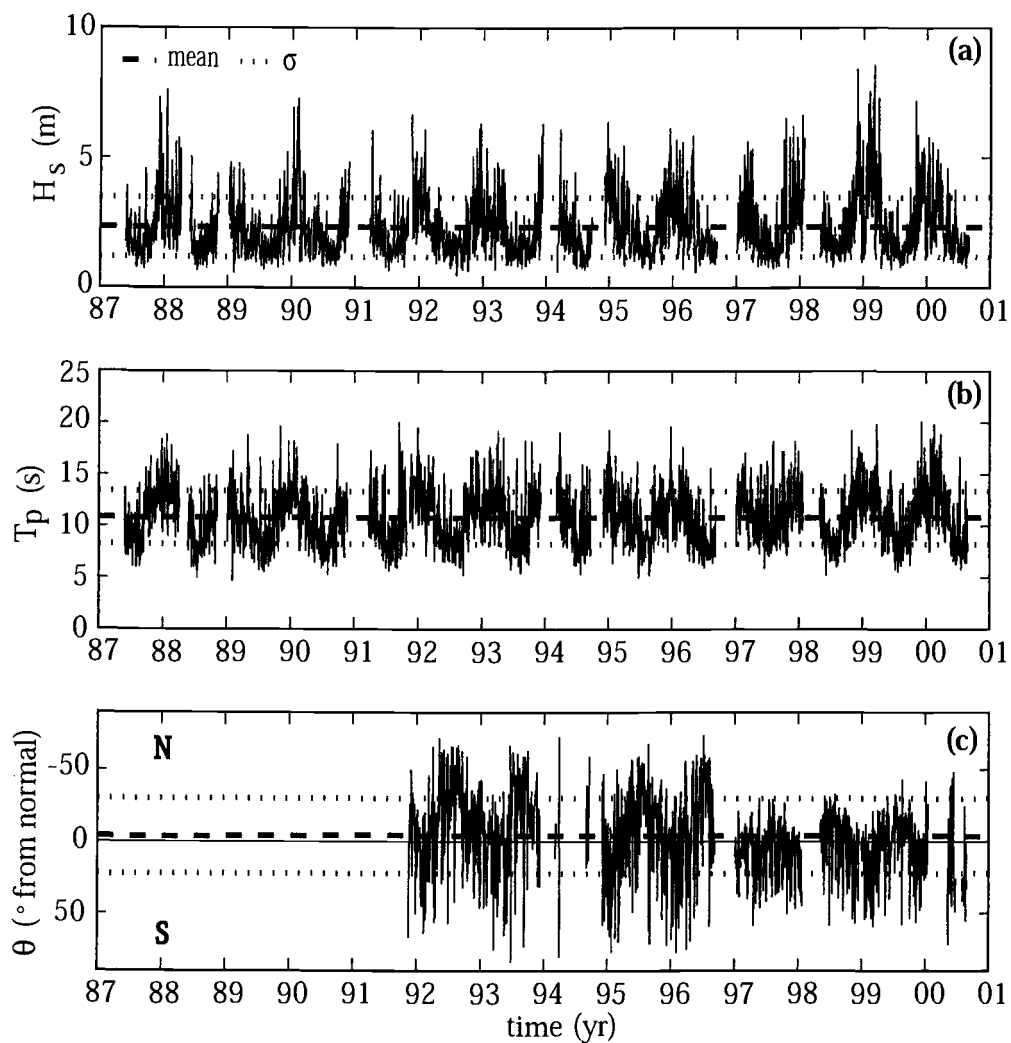


Figure 3.4 The combined records of Newport and CRB daily mean observations of H_s (a), T_p (b), and θ (c) from buoy data. The means and standard deviations over the entire record length for each variable are shown as dashed and dotted lines.

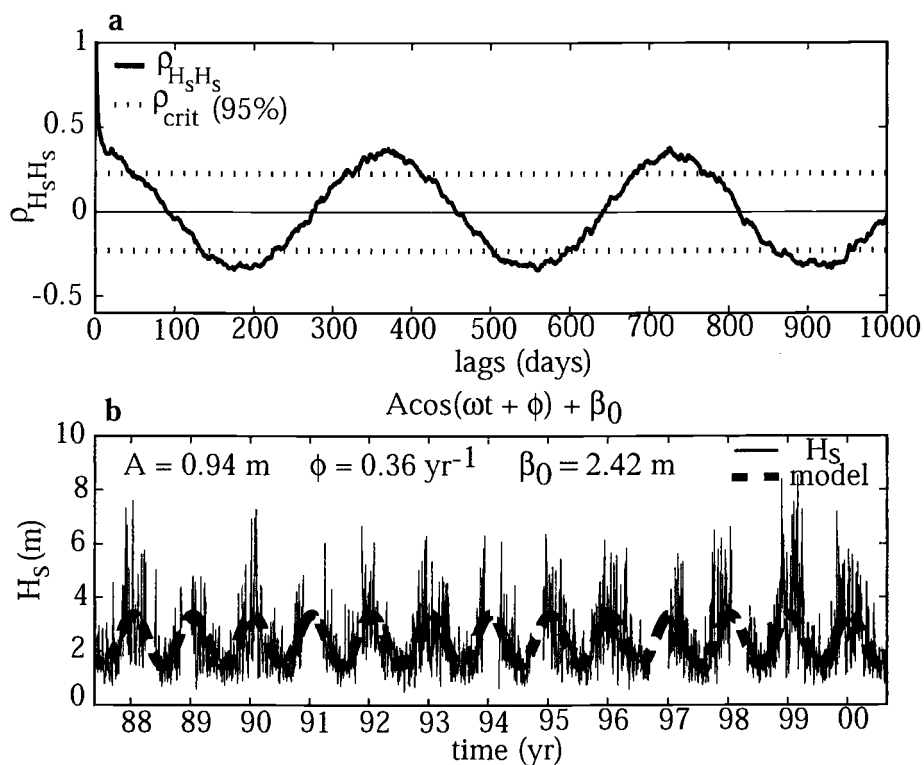


Figure 3.5 Time-lagged auto correlation and annual model for H_S . **a)** The first few cycles of the time-lagged auto correlation for the H_S time series. A mean difference between the significant peaks occurs at 365 days. Values of $\rho_{\text{crit}}(95\%)$ are calculated from estimates of the effective degrees of freedom, $N^* = 75$. **b)** A least squares multiple regression of the annual model for H_S based on the dominant frequency ($\omega = 2\pi/365$) determined in panel (a).

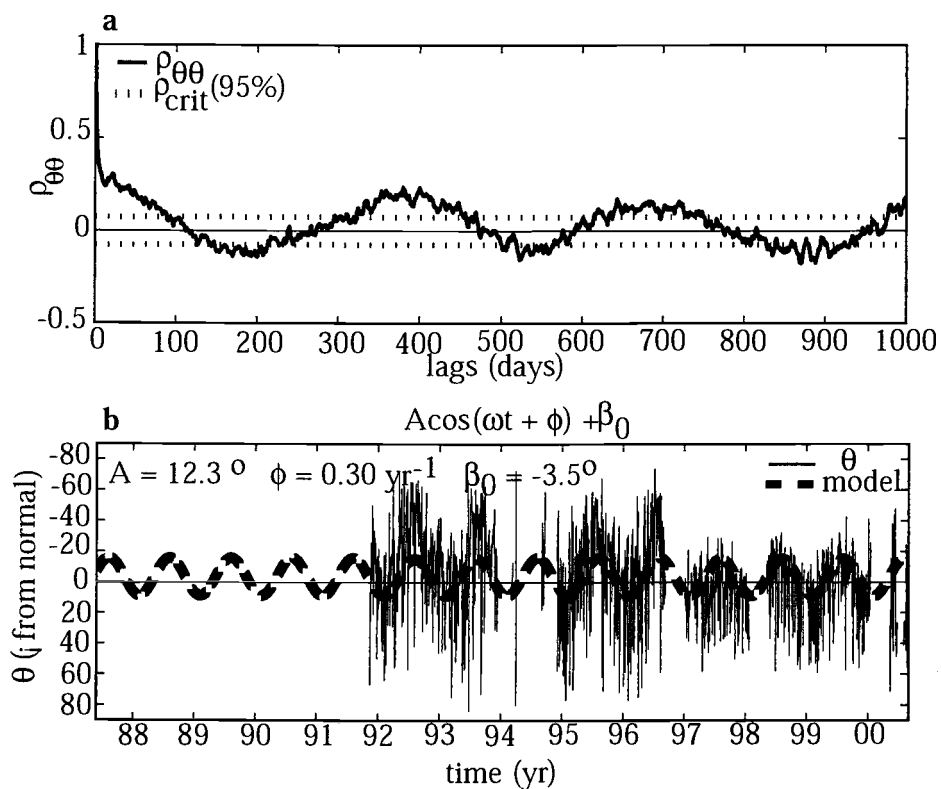


Figure 3.6 Time-lagged auto correlation and annual model for θ . **a)** The first few cycles of the time-lagged auto correlation for the θ time series. A mean difference between the peaks also exists for θ at 365 days. Note the lower $\rho_{\text{crit}}(95\%)$ value than Figure 3.5a, based on a higher estimate of $N^* = 678$. **b)** The multiple least squares regression of the annual model for θ based on the dominant frequency from panel (a).

noise and therefore continuous observations are better correlated. Using the dominant annual frequency ($\omega = 2\pi/365$) uncovered from the auto correlation analysis, the annual component from equation 2 ($A_x \cos(\omega t + \phi_x)$), for each variable is modeled using a least squares regression. The model fit for H_s is significant at the 95% confidence level with $R^2 = 0.34$, $R^2_{\text{crit}} = 0.23$ and $N^* = 75$. Likewise, the annual model fit for θ is also significant at the 95% level with $R^2 = 0.11$, $R^2_{\text{crit}} = 0.075$ and $N^* = 678$. These annual models for H_s and θ coupled with similar analysis of T_p indicate a seasonal pattern with larger, longer period waves approaching from a more southerly direction during the winter season. By expressing the annual wave parameter models in terms of an amplitude (A_x) and phase (ϕ_x) (equation 2, Figures 3.5b & 3.6b), the seasonal increase and decrease of H_s ($A_{H_s} = 0.94\text{m} \pm 0.06$) and seasonal change in direction for θ ($A_\theta = 12.3^\circ \pm 2.0$) are revealed. Similarly, the phase relationship between seasonal wave energy and direction is quantified with ϕ_θ lagging ϕ_{H_s} and ϕ_{T_p} by 24 and 20 days respectively. Therefore, the incident wave energy tends to increase prior to the seasonal change in wave approach, which has an effect on the timing for seasonally based alongshore sediment transport. Model coefficients and other statistics are summarized in chapter 5.

In order to uncover any other important periodic features within the record, the model fit of the annual component from equation 2 is subtracted from the original daily mean time series. An auto correlation of the residuals left by

subtracting the annual model from the original time series failed to resolve any other periodicity within the signal.

The regression analysis reveals a strong seasonality in the wave forcing that has implications for the observed intra-annual variability in the cross-shore sediment fluxes on Agate Beach (section 3.3). Similar to the annual signals in wave forcing based on least squares regression ($A_x \cos(\omega t + \phi_x)$), the seasonal variability in wave forcing can also be modeled as a 12 member set of ensemble averaged monthly statistics $\langle X_e(\text{month}) \rangle$.

$$\langle X_e(\text{month}) \rangle = \frac{1}{N} \sum_{yr} X(\text{month}, yr) \quad (4)$$

$\langle X_e(\text{month}) \rangle$ is calculated as the ensemble average of wave climate observation X , for a common month over the entire record length. The ensemble-averaged annual signals for H_s ($\langle H_{s,e}(\text{month}) \rangle$) and θ ($\langle \theta_e(\text{month}) \rangle$) are shown in Figure 3.7a & 3.7c. Describing the annual signals in terms of an ensemble average over the entire record provides better resolution of the shape of the intra-annual behavior in each parameter. Comparing the annual model of H_s based on least squares regression ($A_x \cos(\omega t + \phi_x)$, Figure 3.5) against the annual model derived from ensemble averaging ($\langle H_{s,e}(\text{month}) \rangle$, Figure 3.7a), shows the difference in the intra-annual shapes of the signals (Figure 3.8). The $\langle H_{s,e}(\text{month}) \rangle$ model shows a more peaky periodic signal with sharp increases in H_s during late fall and early winter months, followed by more shallow drops in wave heights during the spring and early

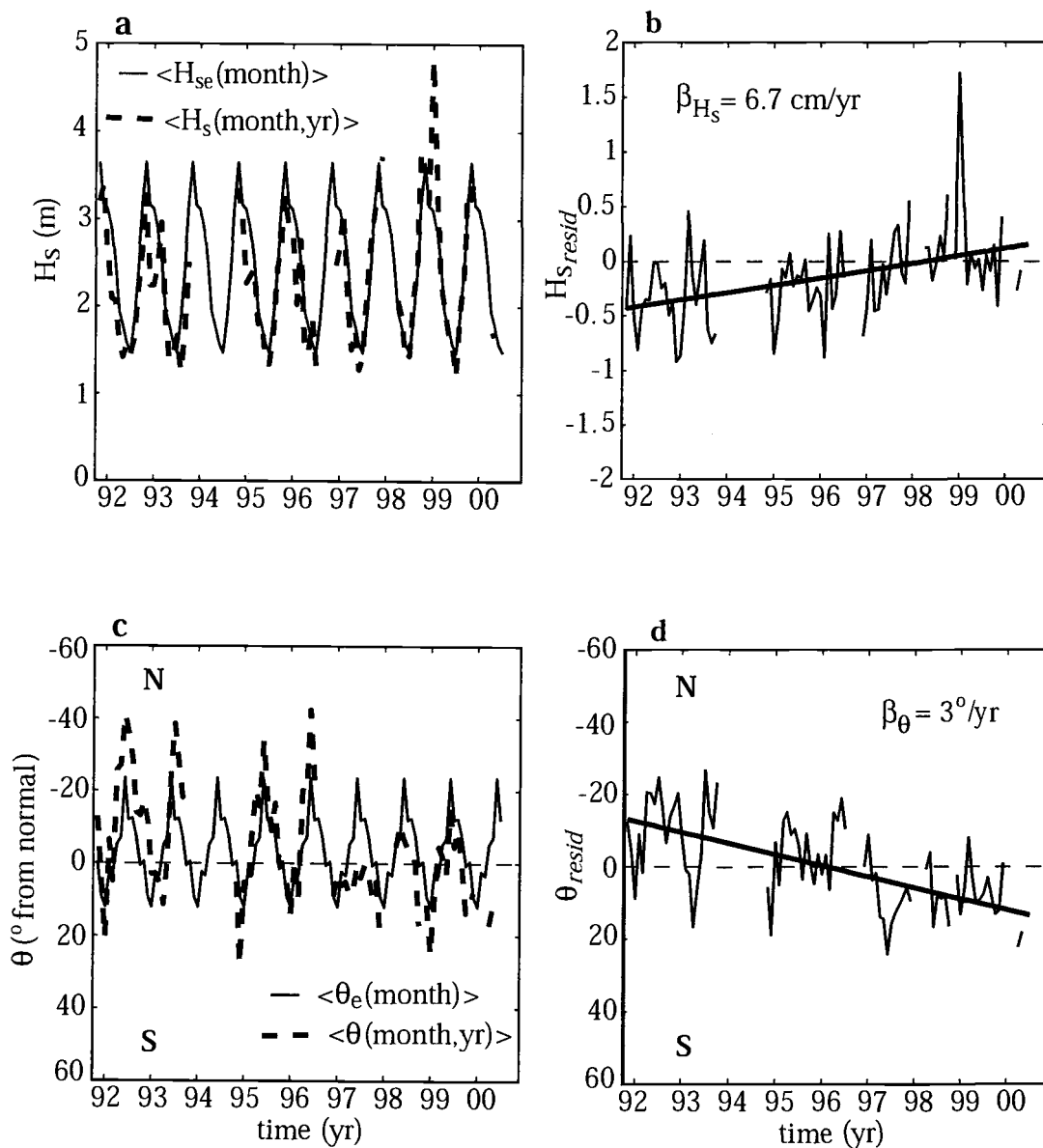


Figure 3.7 Monthly averaged ($\langle X(\text{month, yr}) \rangle$) and repeated, monthly ensemble averaged annual ($\langle X_e(\text{month}) \rangle$) wave climate signals. **a)** Monthly averaged estimates of H_S plotted with the repeated the monthly ensemble averaged annual H_S signal. Note the large change in magnitude and the phase lag during the winter of 1999. **b)** A linear trend fit to the residuals calculated by subtracting ($\langle H_{se}(\text{month}) \rangle$) from ($\langle H_S(\text{month, yr}) \rangle$). **c)** Similar analysis as described in (a) for θ . **d)** A linear trend fit to the residuals for θ indicating a shift in wave approach of 3° south/yr.

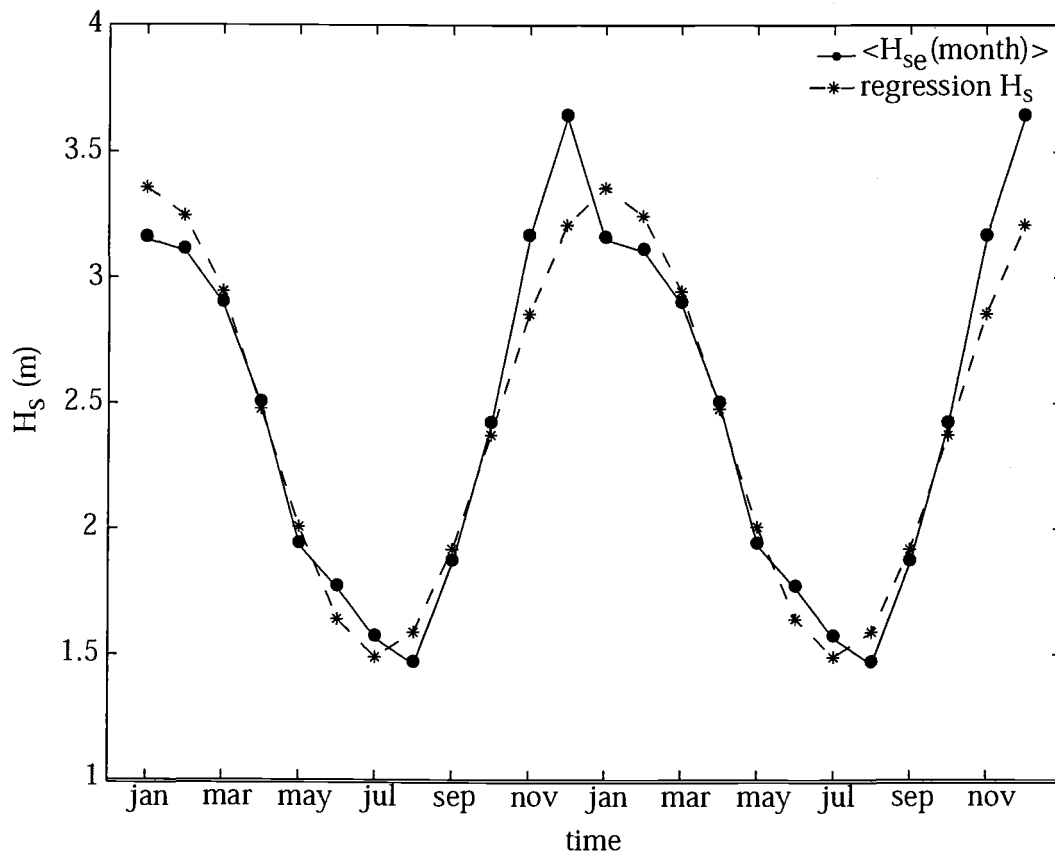


Figure 3.8 The 12 member ensemble averaged annual H_S signal plotted with the periodic regression model for H_S . The ensemble averaged description of H_S resolves the intra-annual behavior produced by a sharp increase in significant wave heights that reaches a larger maximum earlier in the winter than the regression model.

summer. In contrast, the regression based annual signal describes the changes in wave height as a smoother periodic signal, failing to resolve any intra-annual structure.

The interannual variability observed in the wave climate time series provides insight to the wave forcing responsible for the LSCB of Agate Beach. To examine changes in the wave climate over multiple seasons, monthly averages of each variable ($\langle X(month, yr) \rangle$) are calculated.

$$\langle X(month, yr) \rangle = \frac{1}{N_{month}} \sum_{month} X(month, yr) \quad (5)$$

$\langle X(month, yr) \rangle$ consists of the monthly averaged time series of wave observation X as a function of month and year. $\langle X(month, yr) \rangle$ is plotted with the yearly repeated ensemble averaged annual signal $\langle X_e(month) \rangle$ for H_s and θ in Figure 3.7a & 3.7c. Residuals ($X_{resid}(month, yr)$) left by subtracting the repeated $\langle X_e(month) \rangle$ from the $\langle X(month, yr) \rangle$ signal (equation 6) indicates an increase in wave height at a rate of 6.7 cm/yr over the record length (Figure 3.7b).

$$X_{resid}(month, yr) = \langle X(month, yr) \rangle - \langle X_e(month) \rangle \quad (6)$$

The linear trend fit to the H_{sresid} time series is significant at 95% with $R = 0.43$ and $R_{crit} = 0.05$. This result is consistent with the increase noted by Allan and Komar (2000) in their analysis of similar buoy data collected further offshore. The wave direction residuals (θ_{resid}) demonstrate a change in the general angle of approach of the incident wave field at Agate Beach (Figure 3.7d). Over the record length the wave direction has changed to a more southerly approach at a rate of 3°south/yr.

This linear trend is also significant at 95% with $R = 0.63$ and $R_{crit} = 0.05$. The combined change in H_s and θ of the incident wave field as measured by the offshore buoys is alarming. Not only have the significant wave heights increased over time, but their direction has also reoriented to a more southerly approach. These changes in the wave climate are largely influenced by the strong El Niño/ La Niña events that occurred during the winters of 1998-99. The combination of these long-term changes in wave climate have strong implications for interannual variability in the alongshore sediment transport gradients along Agate Beach.

Waves breaking obliquely to the shoreline create an alongshore component of wave momentum flux, known as the radiation stress (S_{xy}), that drives alongshore currents (Bowen, 1969, Longuet-Higgins, 1970, Thornton, 1970).

$$S_{xy} = En \sin \theta \cos \theta \quad (7)$$

E represents the wave energy density, n is the ratio of the wave group and phase velocities, and θ is the wave angle. Komar and Inman (1970) proposed that

$$I_l = KP_l = K(Ecn) \sin \theta \cos \theta \quad (8)$$

where I_l , the immersed-weight alongshore sediment transport rate, is linearly related to the wave power available to transport sediment in the alongshore direction (P_l). K is a dimensionless coefficient, commonly chosen as $K = 0.70$, empirically based on the best fit to existing measurements (Komar, 1998b). (Ecn) represents the wave energy flux per unit crest length with c as the wave celerity. The wave energy is converted to a per unit shoreline basis ($\cos \theta$) and then multiplied by $\sin \theta$ to

represent the portion of the wave power available to drive alongshore transport.

The immersed-weight transport rate (I_l) can be expressed as an alongshore volume transport rate (Q_l)

$$Q_l = \frac{I_l}{(\rho_s - \rho)ga'} \quad (9)$$

where $\rho_s = 2650 \text{ kg/m}^3$ (quartz sand), $\rho = 1020 \text{ kg/m}^3$ (seawater) and $a' = 0.6$ accounts for pore space. Substituting

$$E = \left(\frac{1}{8}\right)\rho g H_{rms}^2 \quad (10a)$$

$$c = \sqrt{g(h + H_{rms})} \quad (10b)$$

where H_{rms} is the root mean square wave height, and choosing a value for $\gamma = H_{rms}/h \approx 1$ in equations (8) and (9), values for the predicted alongshore volume transport rate (Q_l) can be calculated as a function of H_{rms} and θ . Since wave height measurements in this study are recorded as significant wave height H_s , estimates must be converted using $H_s/H_{rms} \approx 1.41$ after Longuet-Higgins, 1952. Finally, assuming alongshore transport of sediment at Agate Beach is dominated by wave driven currents, estimates of Q_l can be made from measurements of significant wave height (H_s) and wave direction (θ).

$$Q_l(t) = 1.2 \times 10^5 H_s^{\frac{5}{2}}(t) \sin \theta(t) \cos \theta(t) \quad (11)$$

The leading coefficient is dimensional and $Q_l(t)$ has units m^3/day . It is important to note that in his analysis, Komar (1970) uses significant wave heights and angles

evaluated at the breaking zone, while we employ significant wave heights and angles measured from inshore buoys.

The daily Q_l time series presented in Figure 3.9a, reveals the seasonal change in the wave-driven alongshore transport direction. During normal years (1992-96), the winter and early spring months are dominated by northward transport, while the summer and fall seasons typically see transport to the south. The 1997-99 portion of the Q_l record reveals not only northward skewness in the transport estimates, but also the dramatic increase in the magnitude of the predicted alongshore transport associated with the El Niño/ La Niña sequence. The Q_l time series is low pass filtered with a one-dimensional loess interpolation scheme using a correlation length scale of 30 days after Schlx and Chelton (1992). The loess interpolation technique will be further discussed in section 3.4. The filtered signal (Q_{lpf}) shown in Figure 3.9b shows the general, long term change in the alongshore transport direction from south to north over the record length. A linear least squares regression fit to Q_{lpf} produces a northward trend of $-22 \text{ m}^3/\text{day}/\text{day}$. This fit is significant at the 95% confidence interval with $\rho = 0.1$ and $\rho_{\text{crit}} = 0.0023$.

Total alongshore transport for any period can be found by integrating equation 11 with respect to time. For example Figure 3.10, a plot of the total annual transport (ψ_{annual}) for each of the study years, shows not only a long-term northward trend, but a significant increase in northward transport in 1999 resulting from a strong La Niña winter. By summing over the entire Q_l record, the net alongshore transport of sediment predicted by wave driven currents is $\psi_{\text{net}} =$

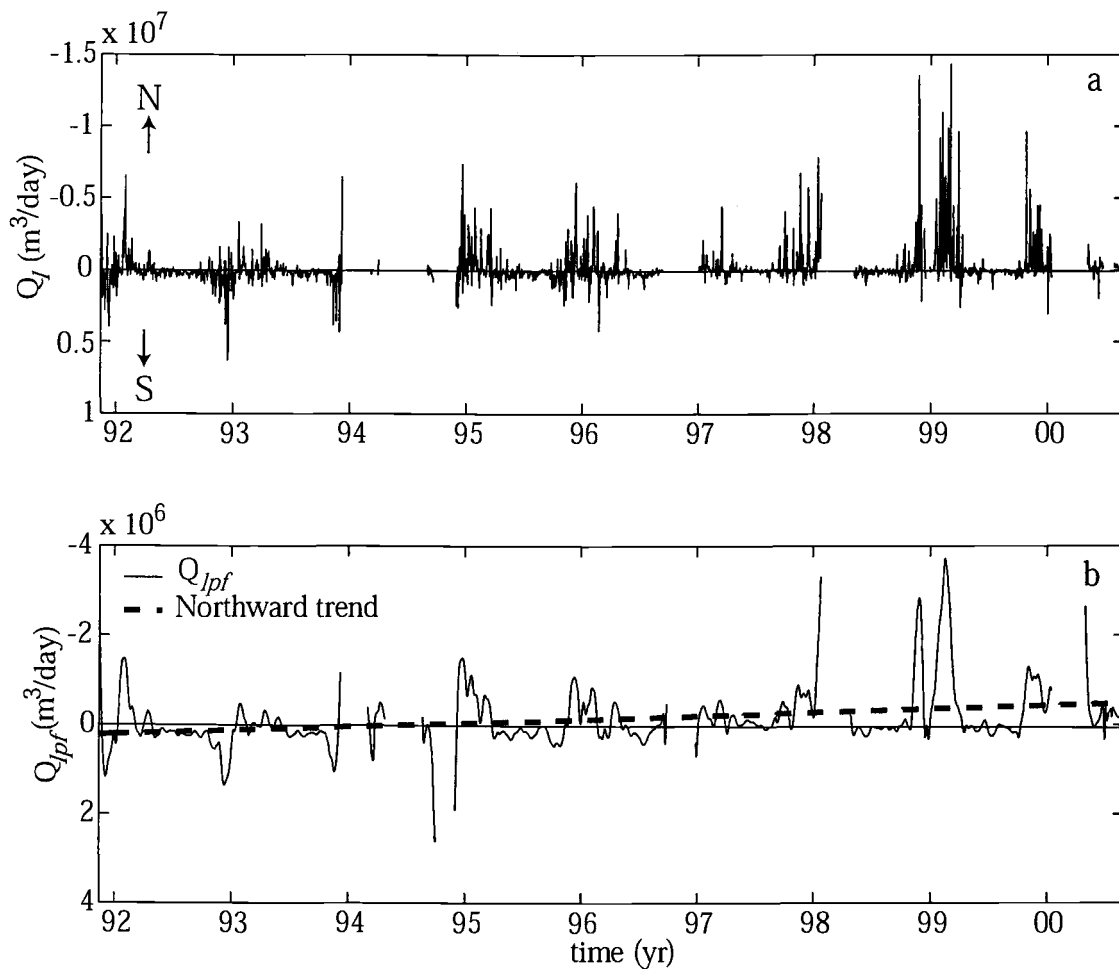


Figure 3.9 **a)** Daily estimates of Q_I from wave data. Note the near equilibrium seasonality in the early part of the record followed by a large increase in the magnitude of predicted northward transport associated with the El Nino/ La Nina sequence. **b)** The low pass filtered Q_{Ipf} time series of predicted alongshore sediment transport flux. A long term linear trend is fit to the Q_{Ipf} signal showing the increase in northward transport over the record length.

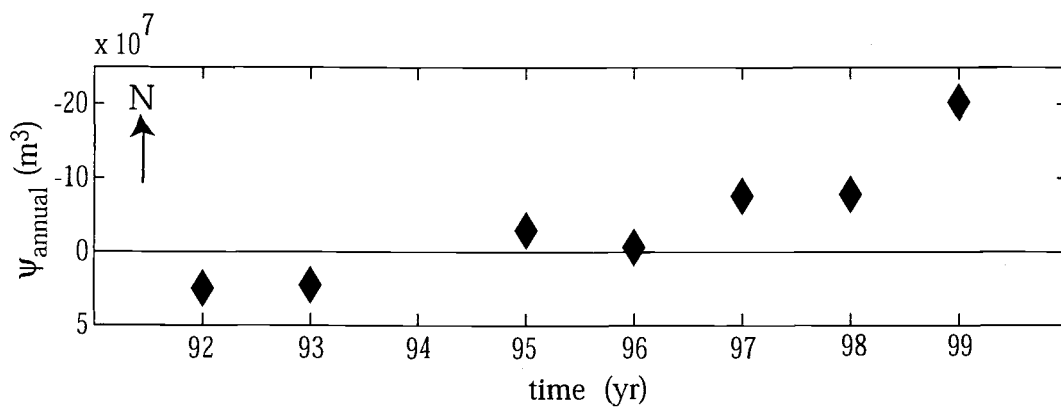


Figure 3.10 The net annual estimate of wave-driven alongshore sediment transport Ψ_{annual} . There is no estimate during 1994 due to a lack of adequate data. Note the strong northward transport during the 1997-98 El Nino/ 1998-99 La Nina sequence.

$2.73 \times 10^8 \text{ m}^3$ to the north. The strong northward trending signal in the record reduces the significance of the limited data gaps. The predicted increase and net northward transport should yield an accretion of sediment at Agate Beach.

3.3 Wind Climate Analysis

Strong winds have an important effect on the morphologic evolution of Agate Beach. Similar to our wave data analysis, a daily mean statistic of wind speed and direction is calculated in order to condense the record. Care was taken not to bias the mean wind direction toward values where the wind velocity was not strong enough to transport sand. From Bagnold (1984), a critical wind velocity threshold (v_{ig}) was established at the anemometer elevation.

$$v_{ig} = 5.75A \sqrt{\frac{\sigma - \rho}{\rho} g d \log \frac{z}{k}} \quad (12)$$

For equation 12, σ is the density of the sand (2.65 g/cm^3 for quartz), A is a coefficient equal to 0.1 for air, ρ is the density of air (0.0013 g/cm^3), d is the sediment grain size (0.2 mm), k is a measure of surface roughness ($k = d/30$), and z is the height above the beach surface where the wind is measured (9.4 m). Using this relationship, a wind velocity threshold value of $v_{ig} = 7 \text{ m/s}$ was used to filter data collected by the anemometer on the south Yaquina Bay jetty. Data with wind speeds lower than this threshold value were removed from the time series prior to the calculation of daily mean statistics for wind velocity and direction.

A portion of the monthly averaged record from June 1995 through February 2001 is shown in Figure 3.11. The threshold filtered, daily mean wind time series reveals two dominant types of variability corresponding to the seasonal wind patterns discussed in section 2.1. The first pattern consists of strong winds from the southwest that occur during winter months as storms and large waves impact the beaches. Due to saturation of the beach sediments from rainfall and swash, this mode contributes little to the observed sediment fluxes. The second pattern is comprised of late spring, summer, and early fall months that are dominated by weaker, but still substantial winds approaching from the northwest. It is these northwest, summer winds that contribute most to the overall sediment transport and formation of the dune field that fronts the sea cliffs.

3.4 Topographic Data Analysis

3.4.1 Gridding and Transformation

In order to analyze temporal and spatial scales of variability within the topographic survey records, the elevation data from each survey must be interpolated to a fixed horizontal grid in the local coordinate system. The surface gridding is accomplished using a two dimensional form of the Loess filter interpolation technique after Schlax and Chelton (1992). The grid nodes used in this analysis are spaced 10 m apart in the cross-shore and 20 m in the alongshore. The interpolation scheme is based on fitting a local quadratic beach surface model

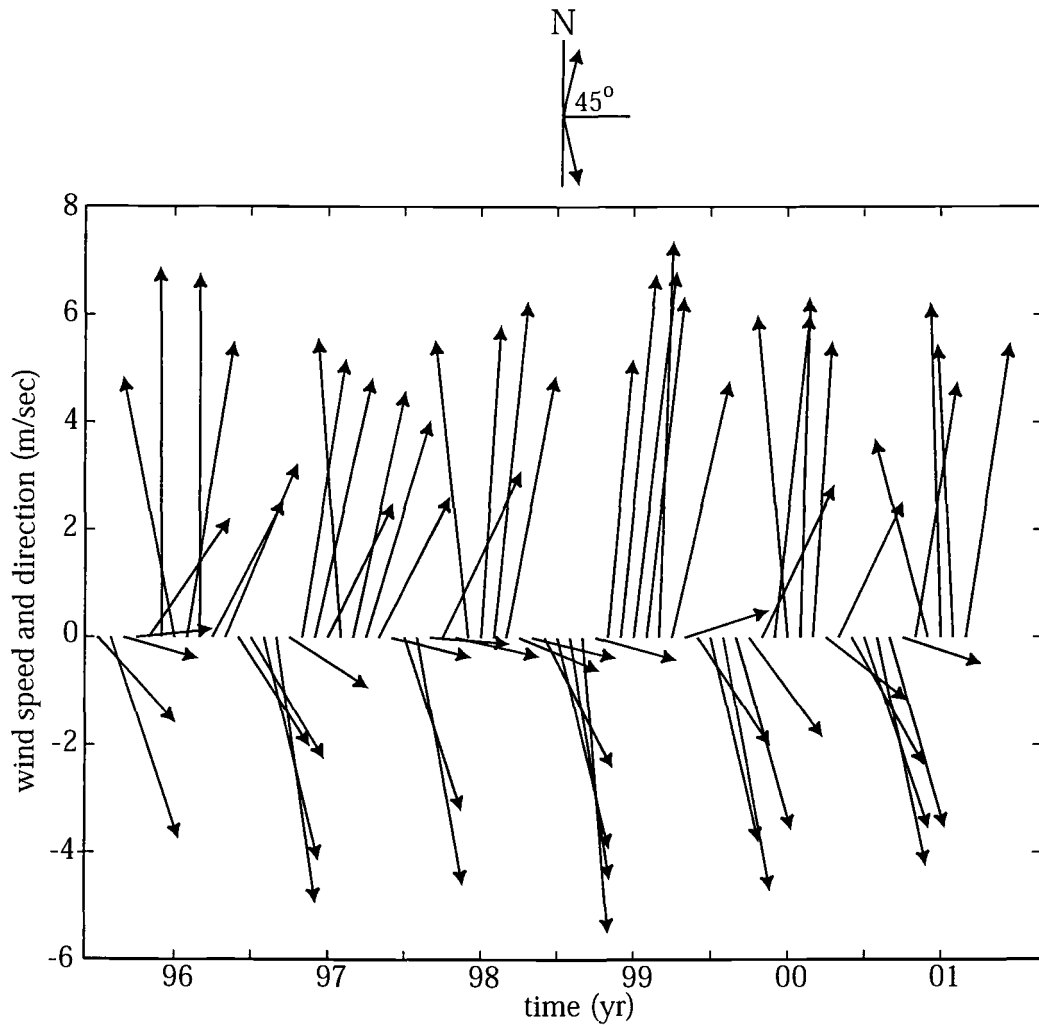


Figure 3.11 Threshold filtered, monthly averaged wind speed and direction from an NDBC anemometer fixed 9.4 m above mean sea level on the south Yaquina Bay jetty. Notice the seasonal patterns of powerful winds from the southwest during the winter followed by strong summer winds from the northwest.

to the survey points by minimizing mean square deviations between the model and survey data. Besides providing elevation estimates at the grid nodes, the Loess filter interpolation technique supplies smoothing for variability at scales shorter than a user determined cutoff. This cutoff determines the wavelength of features that can be resolved in the interpolated field. Isotropic correlation length scales of 100 m were applied in order to limit the occurrence of missing interpolation estimates within the time series resulting from sparse sampling. This smoothing allows resolution of features with wavelengths 200 m or more in the cross-shore and alongshore directions (Figure 3.12a). Areas of the beach with short scale variability (e.g. the seasonal dune field discussed earlier) are effectively smoothed over. Most important, the Loess technique provides error estimates due to interpolation uncertainty (Figure 3.12b). High errors in the interpolation field can result from large spatial gaps between survey observations. However, in the interior of the sampling region the typical interpolation uncertainty produced by the Loess technique at the previously mentioned smoothing scales is $O(0.005\text{m})$. Similar to Plant and Holman (in review), grid nodes with interpolation errors above 0.1m have been removed from each gridded survey set.

The alongshore curvature of Agate Beach produces inconsistencies in the directions for cross-shore and alongshore estimations of sediment flux within the current local coordinate system (Figures 2.2). It is necessary to remove this curvature in order to get at the local cross-shore and alongshore orientations of the beach. First, a circle is regressed on to the time averaged horizontal position of the

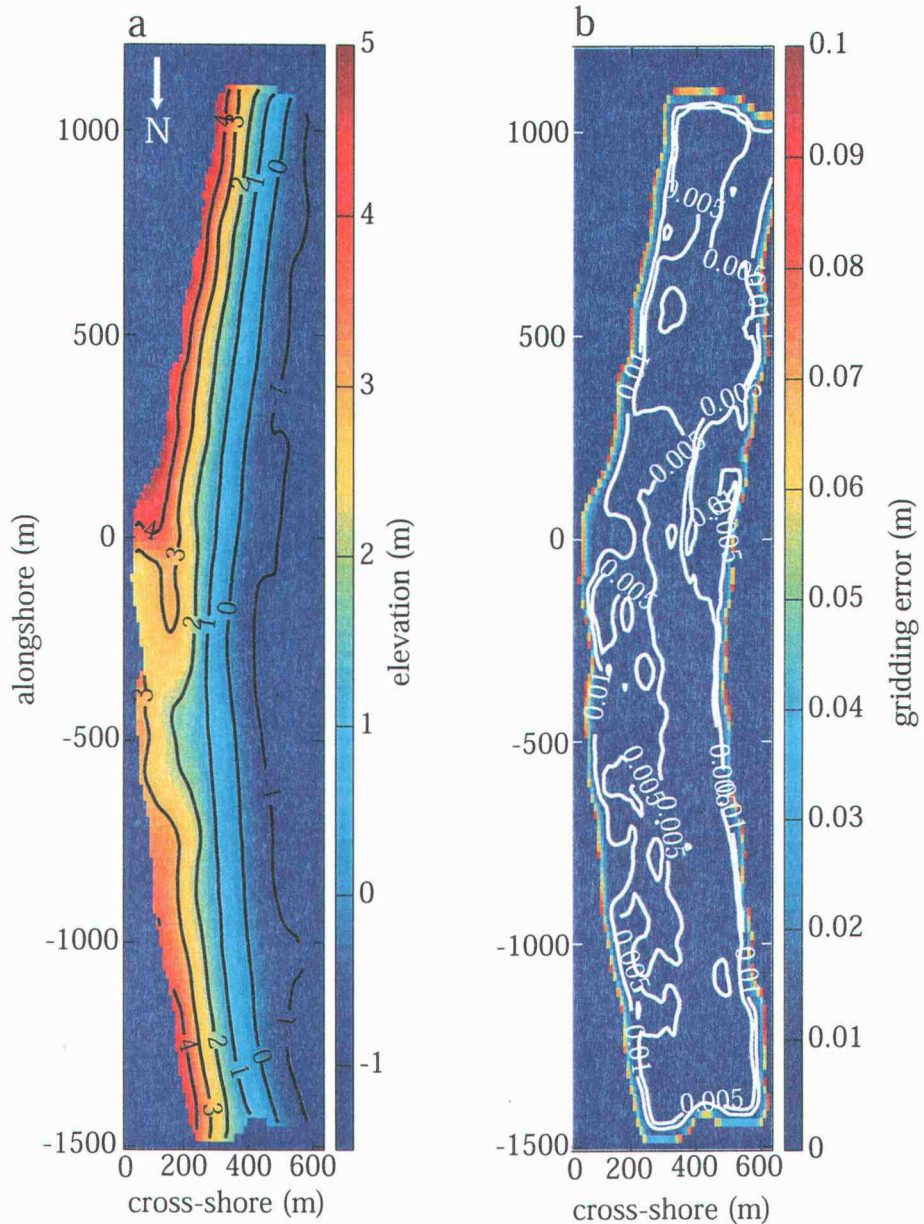


Figure 3.12 RTK-GPS gridded data and interpolation errors from a topographic survey of Agate Beach on November 11, 2000 **a)** The gridded beach surface with nodes separated by 10 m in the cross-shore and 20 m in the alongshore. The colors represent elevation, and contours are shown in 1 m intervals. **b)** The error calculation at each grid node due to interpolation uncertainty. Note the extremely low error in the center of the survey region.

1m elevation contour (Figure 3.13). The radius of the circle fit (r_0) is extended to contain the survey region within the circle boundary (r_{ext}) (Figure 3.14a). Next, the local coordinate system origin is translated to the center of the circle. We then define a domain D as the region bounded by the circle and transform the local coordinate system into complex space Z .

$$Z = x + iy \quad (13)$$

The transformation of the domain D in complex Z space, to a domain D^* in complex space W , where the cross-shore position of elevation contours remains constant, is done using a linear fractional transformation (O'Neil, 1995, Figure 3.14b).

$$1. \text{ Normalization to the unit disk} \quad Z' = \left(\frac{1}{r_{ext}} \right) Z \quad (14a)$$

$$2. \text{ Fractional Transformation} \quad W' = T(Z') = -\frac{(Z' + 1)}{(Z' - 1)} \quad (14b)$$

$$3. \text{ Magnification and Translation} \quad W = r_{ext} W' + iy_0 \quad (14c)$$

y_0 = alongshore center of the circle in the original local coordinate system

The black cross-hatched lines in Figure 3.14a are separated by 50 m in the cross-shore and alongshore directions. Figure 3.14b shows the minimal distortion of those regularly spaced grid lines resulting from mapping Z space to W space. The domain of interest, D^* , is a small area with respect to the total area of the circle and

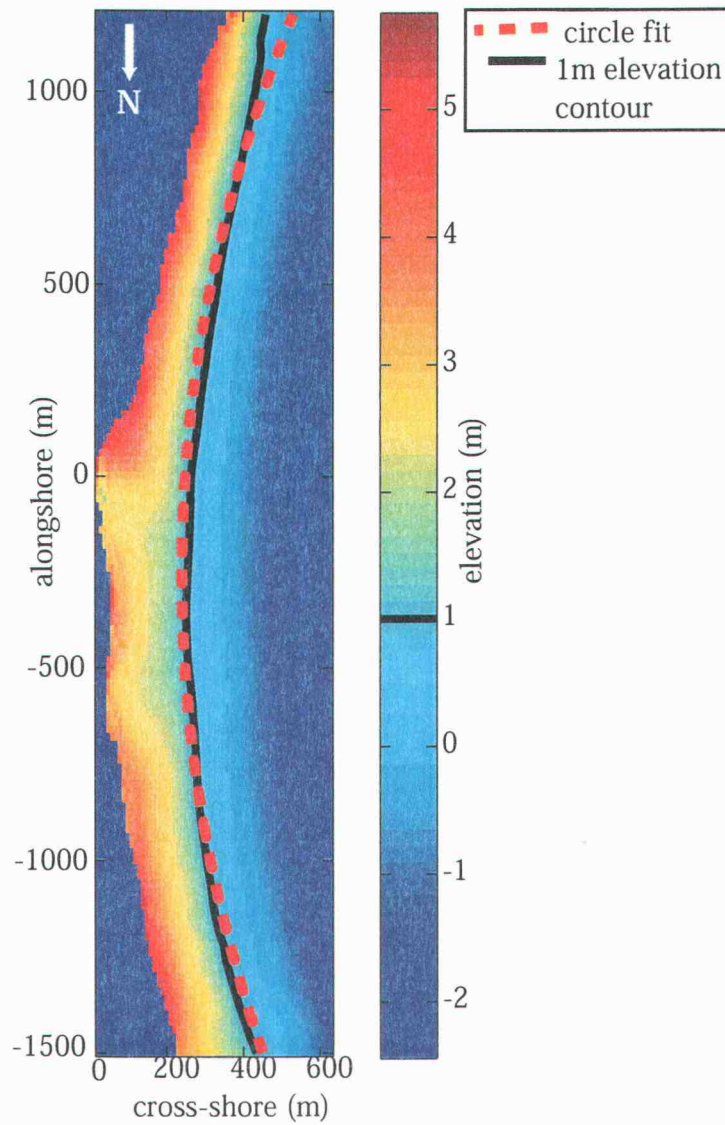


Figure 3.13 The time averaged gridded beach surface over the 27 survey topographic record.

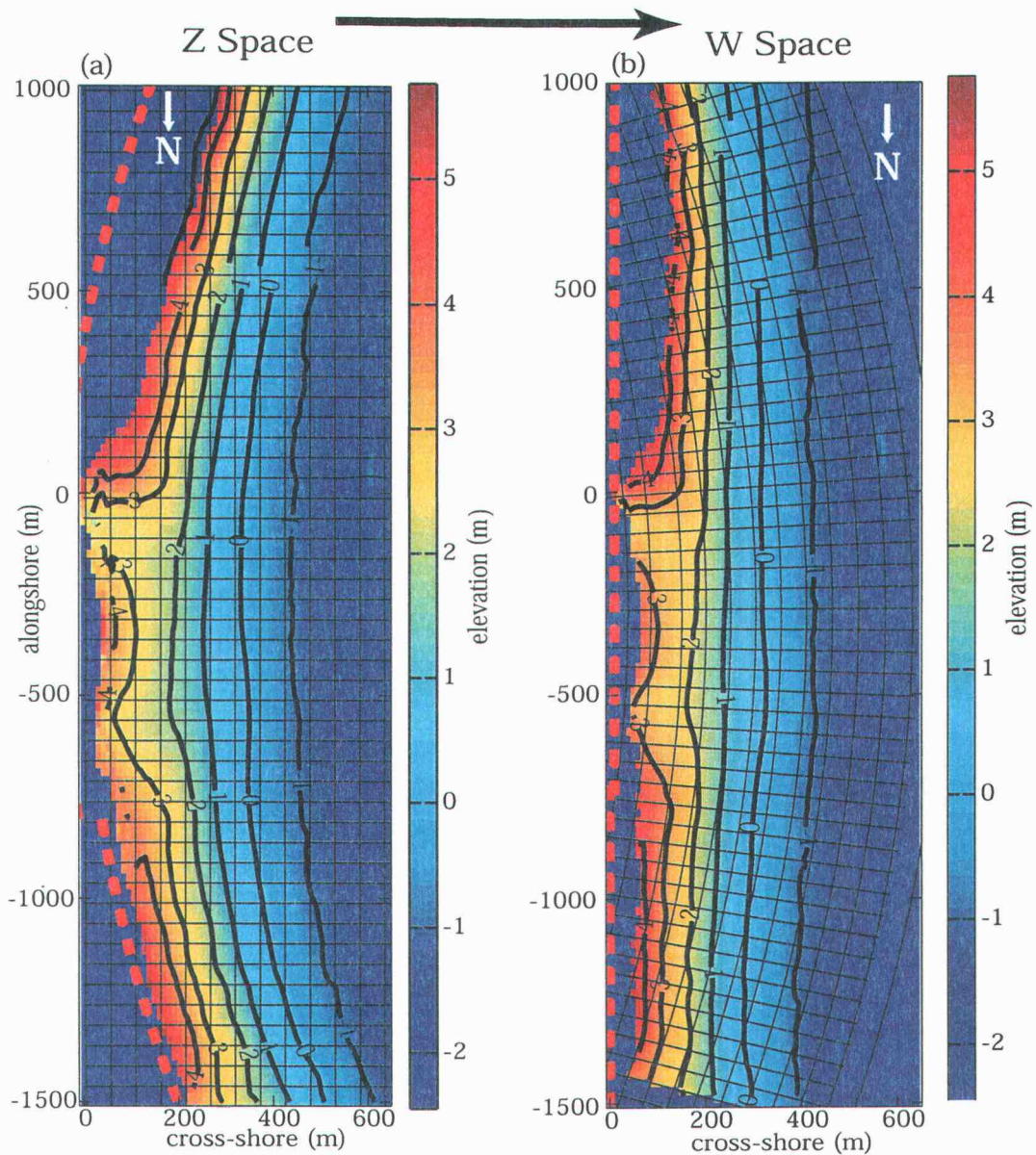


Figure 3.14 The transformation of the mean beach surface from Z to W space. **a)** The mean beach surface with elevation contours and the circle boundary of the beach region dashed in red. Note the alongshore curvature of the elevation contours in Z space. **b)** The mapping of the mean beach surface into W space, where the elevation contours and circle boundary become lines. Cross-hatched lines in (a) are spaced 50m in the cross-shore and alongshore. The same pattern is mapped into W space to show the minimal amount of horizontal distortion caused by the mapping.

is also located very near the circle boundary. Because of these two factors, the maximum horizontal distortion, $O(0.1 \text{ m})$, caused by the linear fractional transformation occurs near the alongshore extremes of the domain, D^* . Here, we define distortion as the change in unit length in the x and y directions caused by the transformation.

3.4.2 Beach Surface Change Analysis

After the alongshore curvature of the beach has been removed, the patterns of local cross-shore and alongshore sediment flux are more readily identifiable. Figure 3.15 shows mean, standard deviation, and skewness maps of the gridded beach surface over the complete survey time series. Grid nodes with less than 50% of the total number of observations have been removed from all of the remaining analysis (Figure 3.16). The channel morphology related to Big Creek and Little Creek near $y = 0 \text{ m}$ and $y = -500 \text{ m}$ are well-resolved features in the time averaged beach surface. Besides these two areas influenced by the creeks, the mean beach surface shows little alongshore structure. The standard deviation map in Figure 3.15b illustrates the spatial structure of the beach surface variability over the 6 year record length. It is important to note that the beach response is not cross-shore uniform. Instead, Agate Beach exhibits increased amounts of surface variability located in the backshore near Big Creek and in 2 alongshore parallel bands around $x = 200 \text{ m}$ and 400 m . The patch of high variability associated with Big Creek ($0 > y > -600 \text{ m}$) is due to the migration of the creek channel to the north (observed in

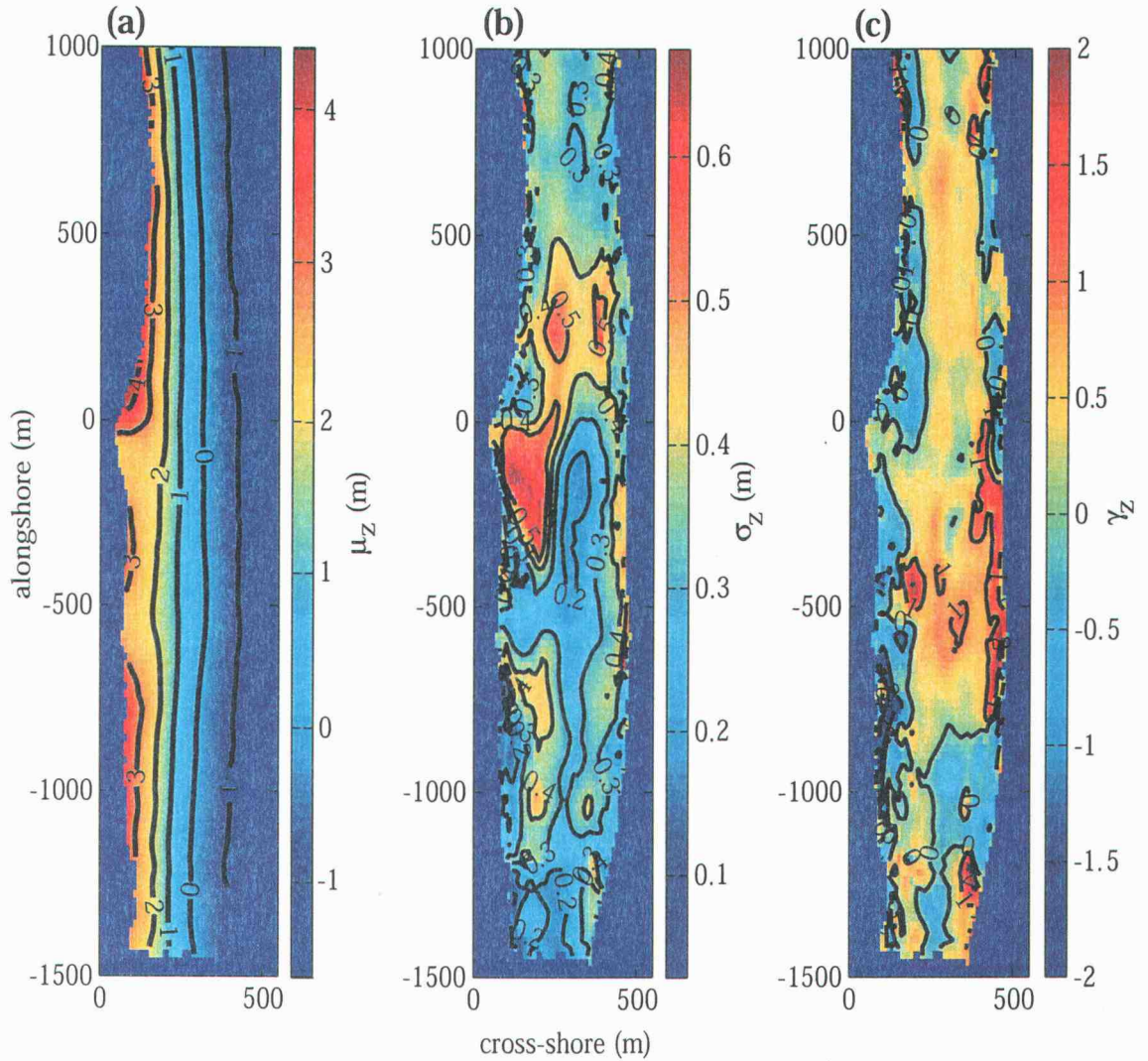


Figure 3.15 Statistics of surface variability at Agate Beach over the survey record length. The alongshore curvature of the beach has been removed. **a)** The time averaged beach elevation surface, μ_z **b)** The standard deviation map with respect to z , σ_z , illustrates the alongshore and cross-shore structure of surface changes. **c)** The skewness map, γ_z , is dominated by positive values, indicating that most of the observations throughout the record occur below the mean beach surface elevation.

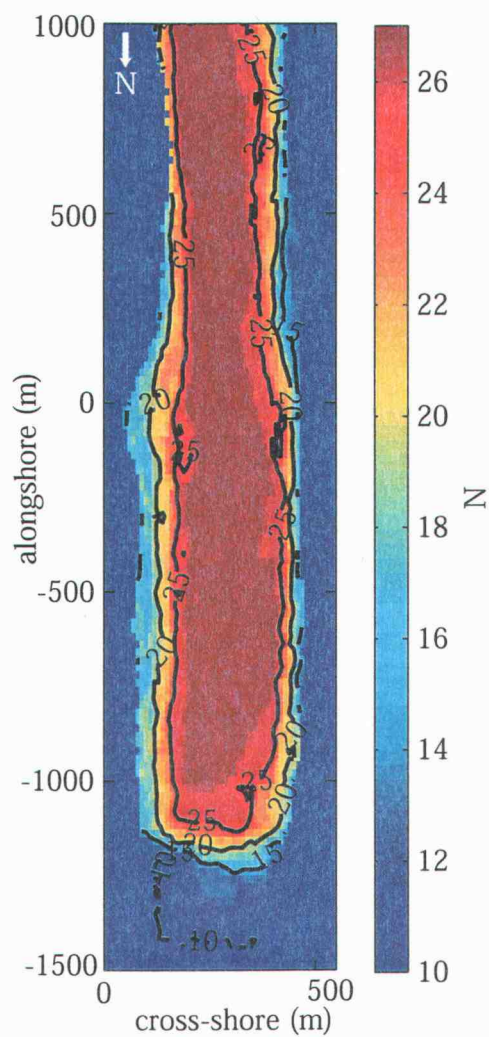


Figure 3.16 The number of observations (N) at each grid node over the 27 survey record length.

the Argus video record in 1996) as well as channel cutting and fill from large seasonal changes in rainfall and discharge. The alongshore bands of increased variability are good indicators as to the cross-shore behavior of the beach response. In the cross-shore direction, there are distinct locations with a greater sediment response to changes in wind and wave forcing that will be discussed later. The skewness map (Figure 3.15c) indicates that the majority of the observations at each grid cell are positively skewed. Therefore, the majority of the beach is more often observed below the time averaged beach surface elevation. This is a result of the irregular sampling interval shown in Figure 2.4. Because 16 of the 27 topographic surveys are found in the 1995-96 survey series, skewness statistics are biased toward a beach containing less sediment. The range map shown in Figure 3.17, is calculated by subtracting the minimum elevation value from the maximum value at each grid point in the survey record. By summing over the range map a volume difference of $1.30 \times 10^6 \text{ m}^3$ quantifies the dynamic volume of sediment involved in transport processes along the beach over the survey record length.

Removing the alongshore curvature of the beach also allows us to make alongshore averaged calculations of the mean beach profile, standard deviation, and skewness as a function of cross-shore position (Figure 3.18). The alongshore and time-averaged profile illustrates the shallowing of the beach slope with increasing offshore distance that is typical of beaches exposed to high incident wave energies. A plot of the alongshore-averaged standard deviation, σ_x , shows two dominant bands of beach elevation variability in the cross-shore direction (Figure 3.18b).

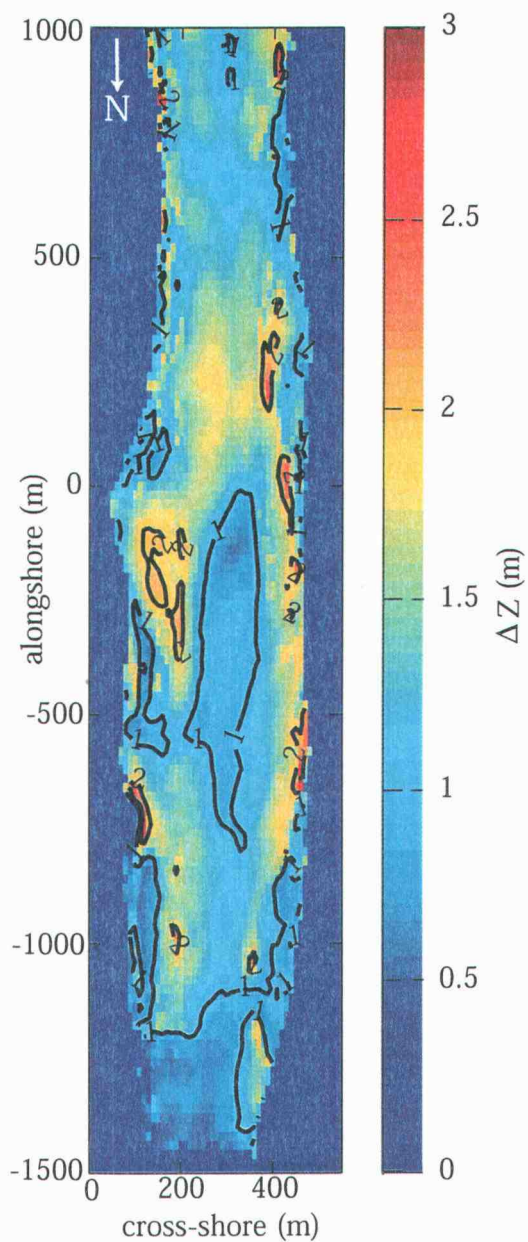


Figure 3.17 The range in elevation at each grid node calculated by subtracting the minimum elevation from the maximum elevation observed throughout the survey time series. Note some regions of change up to 3m in elevation.

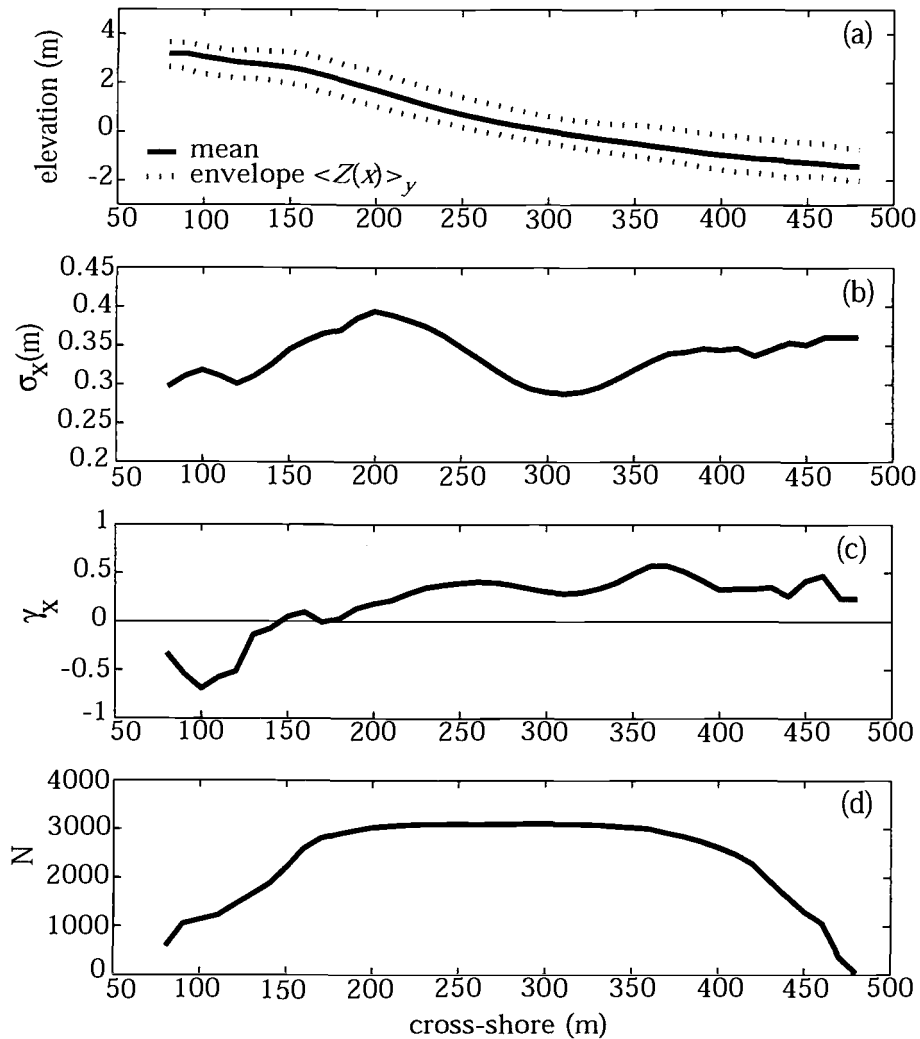


Figure 3.18 The alongshore averaged statistics of the Agate Beach survey time series. **a)** The mean beach surface elevation profile. **b)** The standard deviation profile reveals a decrease in surface variability around $x = 300$ m, surrounded by two distinct bands of higher variability. **c)** The skewness profile shows a switch from negative to positive values at $x = 150$ m. The beach seaward of that point is more often observed below the mean surface elevation, while areas landward are more often found above the mean elevation profile. **d)** The number of observations at each cross-shore location.

The band from $150 < x < 275$ m will be shown later to correspond to the wind-driven, seasonal dune field that develops during summer months. The second band of increased variability occurs seaward of $x = 300$ m. This area is continually under the influence of swash and hydrodynamic sediment transport processes directly related to the offshore wave climate.

The alongshore averaged skewness profile, γ_x , (Figure 3.18c) reveals some cross-shore structure with a node at $x = 150$ m. Seaward of $x = 150$ m the skewness remains positive, indicating that the majority of observations found at cross-shore positions greater than $x = 150$ m lie below the mean elevation for that position. On the contrary, all grid nodes landward of $x = 150$ m are negatively skewed.

Therefore, around $x = 150$ m there is a node where the beach surface responds differently on both the landward and seaward sides. It is also worth noting that this result may be a product of the bias created by inequality in sampling between the two survey series (Figure 2.4).

Perhaps a more interesting way to analyze the variability in the survey data is by examining the variation of statistics with vertical elevation. Gridded elevation values throughout the survey record are binned in 5 cm increments from $z = -2.525$ m to $z = 5.025$ m. The time averaged cross-shore position and range of each elevation bin are plotted in Figure 3.19a showing the gently sloping nature of the mean beach surface. The standard deviation profile with respect to elevation, σ_z , (Figure 3.19b) reveals a decrease in variability near the 1 m elevation contour. This dip in the profile indicates an elevation contour in the beach surface that

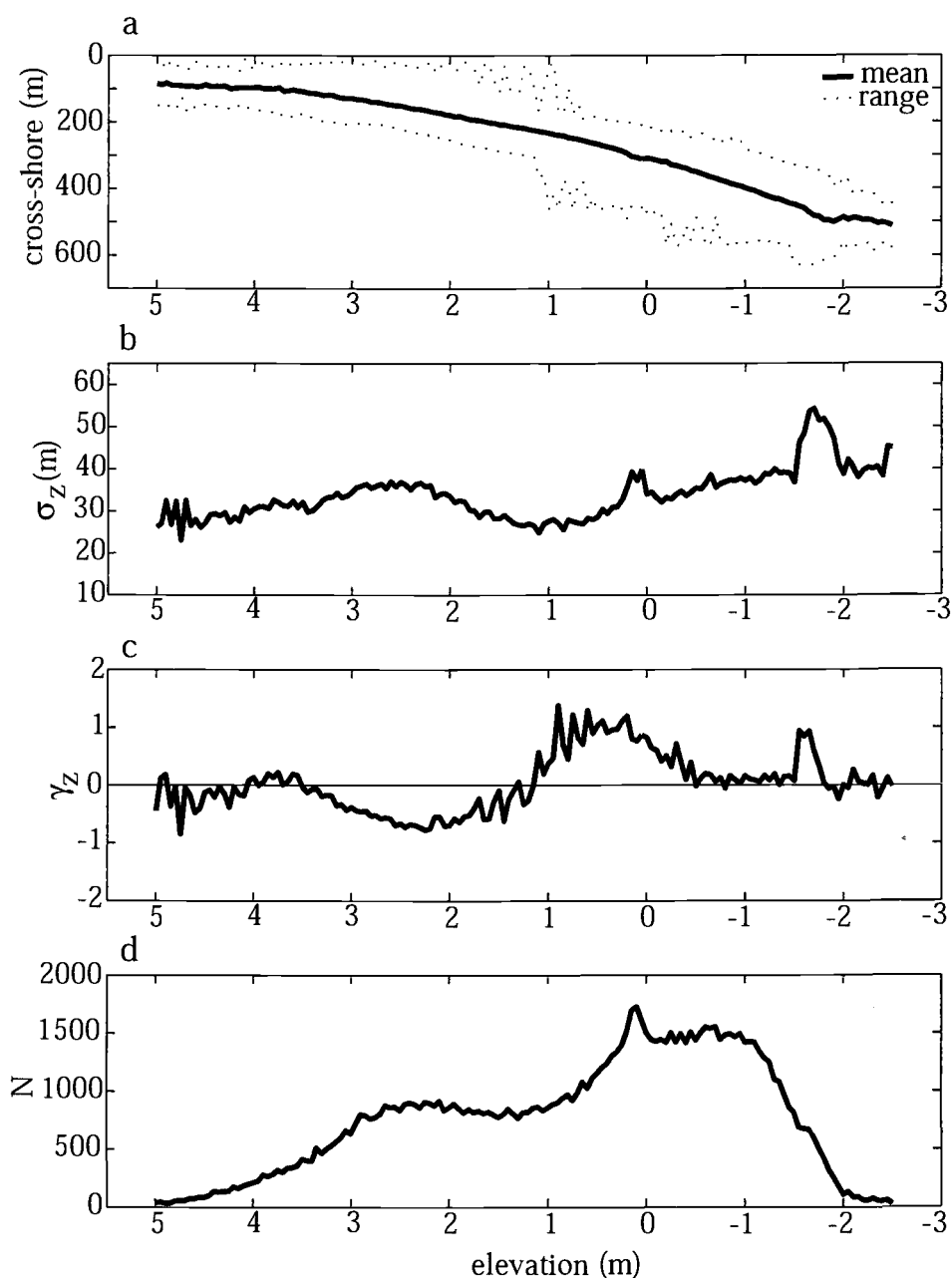


Figure 3.19 Statistics of Agate Beach as a function of surface elevation. **a)** The time-averaged cross-shore position and range of each 5 cm elevation bin. **b)** The standard deviation for each elevation bin reveals a decrease in cross-shore variability near the 1 m elevation contour. **c)** Similarly, the skewness profile resolves a node near the 1 m elevation contour. Elevations above 1 m are negatively skewed while elevations below 1 m are positively skewed. **d)** The number of observations in each elevation bin.

responds less to forcing than both higher and lower elevations. Furthermore, the skewness map with respect to elevation, γ_z , (Figure 3.19c) reveals a node around the same 1 m elevation contour. Elevations higher than the 1 m contour are more regularly observed seaward of their mean position due to negative skewness, while elevations lower than 1 m are more often observed landward of their mean position as a result of positively skewed values. Again, these results may also be a product of sampling bias shown in Figure 2.4.

Analysis of the survey data with respect to elevation shows that the beach surface responds in distinct bands of variability on either side of the 1 m elevation contour. Interestingly, the NOAA tidal gauge in Yaquina Bay estimates mean high water (MHW) at $z = 1.076$ m and mean higher high water (MHHW) at $z = 1.283$ m. The bands of increased variability around the 1 m elevation contour suggest an interesting separation in the beach profile response. The cross-shore profile behaves as the combination of a wave driven response that tapers away above MHW, and an aeolian dune response that is limited to the region above MHW.

An empirical orthogonal function (EOF) analysis of the survey record identifies the spatial and temporal patterns of beach surface variability (Winant et al., 1975, Davis, 1976). Due to large changes in beach surface elevations between the 1995-96 and 2000-01 survey series, the elevations from each survey are normalized to unit range in order to better resolve the intra-annual patterns of surface variability.

The EOF decomposition of the survey record produces two distinct modes explaining 34% and 21% of the normalized variability (Figure 3.20). In our previous analysis of the topographic surface data we have shown where the beach responds to changes in forcing. The EOF analysis not only decomposes the variance into independent spatial patterns of variability, but also provides a time signature related to these modes of variance.

The spatial pattern of the first mode is relatively alongshore uniform suggesting a response due to cross-shore fluxes of sediment. The alongshore mean of the spatial pattern outlines a cross-shore profile that is dominated by a backshore beach response (Figure 3.20a). This mode describes the dune field that emerges in the backshore next to the seacliff during the drier summer months. The temporal pattern of the first mode is correlated to an annual amplitude signal that is more readily visualized in Figure 3.21. In the top panel the first year survey time series (1995-96) of the EOF mode 1 amplitude signal is shown. During the summer and early fall months, the amplitude of the first mode increases, making the growth of the dune field in the backshore an important part of the beach surface variability. Along with the (1995-96) amplitude time series of the first mode, a periodic, annual ($\omega = 2\pi/365 \text{ days}^{-1}$) signal is plotted to show the seasonal nature of the dune mode.

In the lower panel (Figure 3.21b), the corresponding monthly statistic for wind speed and direction are plotted for a comparison with the dune mode amplitude time series. When the wind is strong and from a southerly direction, the amplitude of the dune mode decreases. Figure 3.22 plots the monthly mean

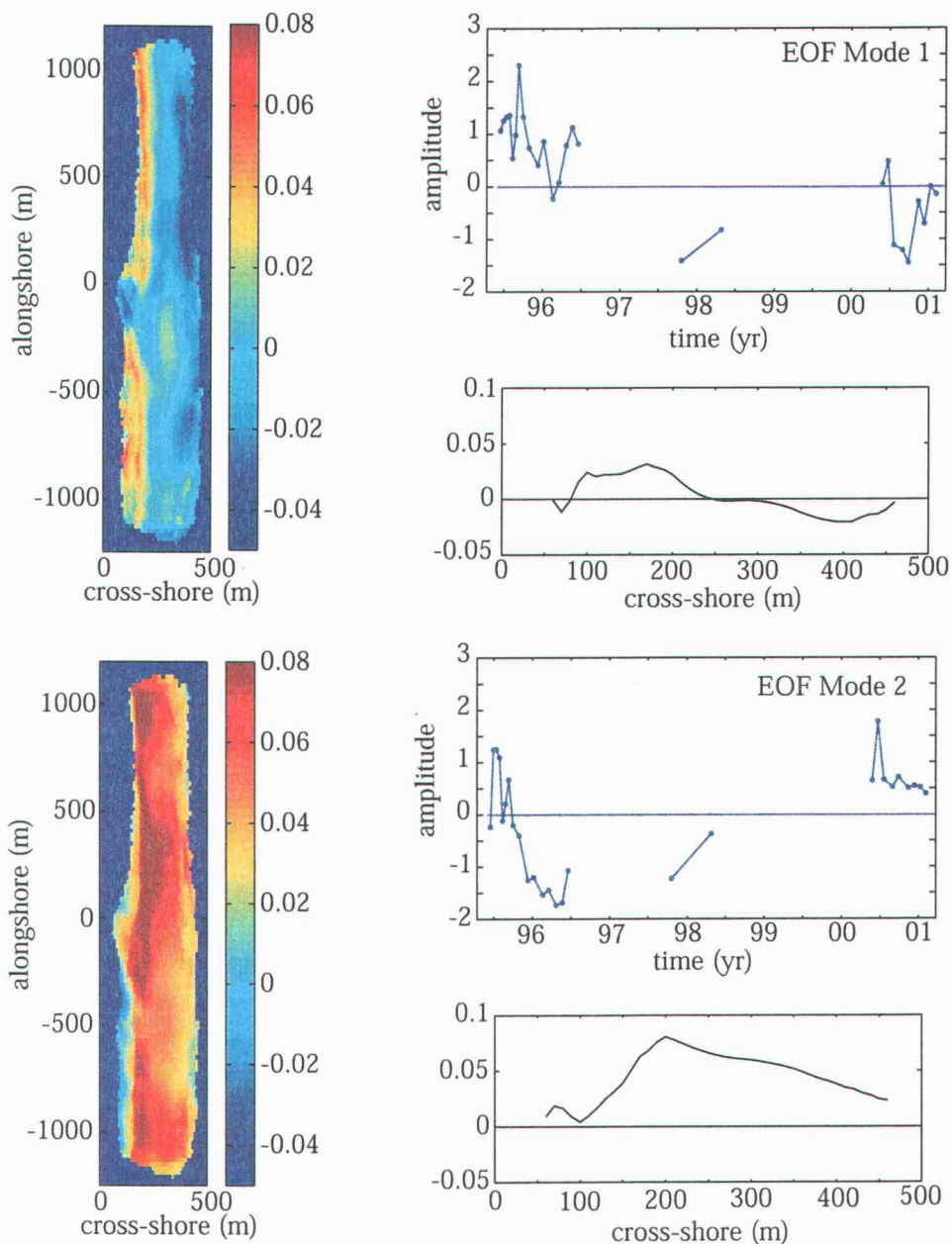


Figure 3.20 EOF analysis of the normalized survey record reveals two distinct modes of surface variability. The first mode (34% of the variance) suggests a pattern related to the seasonal backshore dune field that forms during the summer months. An alongshore average of the mode shows the cross-shore structure of the dune pattern. The amplitude time series of the first mode reveals a seasonal cycle related to dune growth in summer and loss of sediment in this region during winter. The second mode (21% of the variance) appears to be related to the seasonal changes in the rest of the beach surface elevations outside of the dune area.

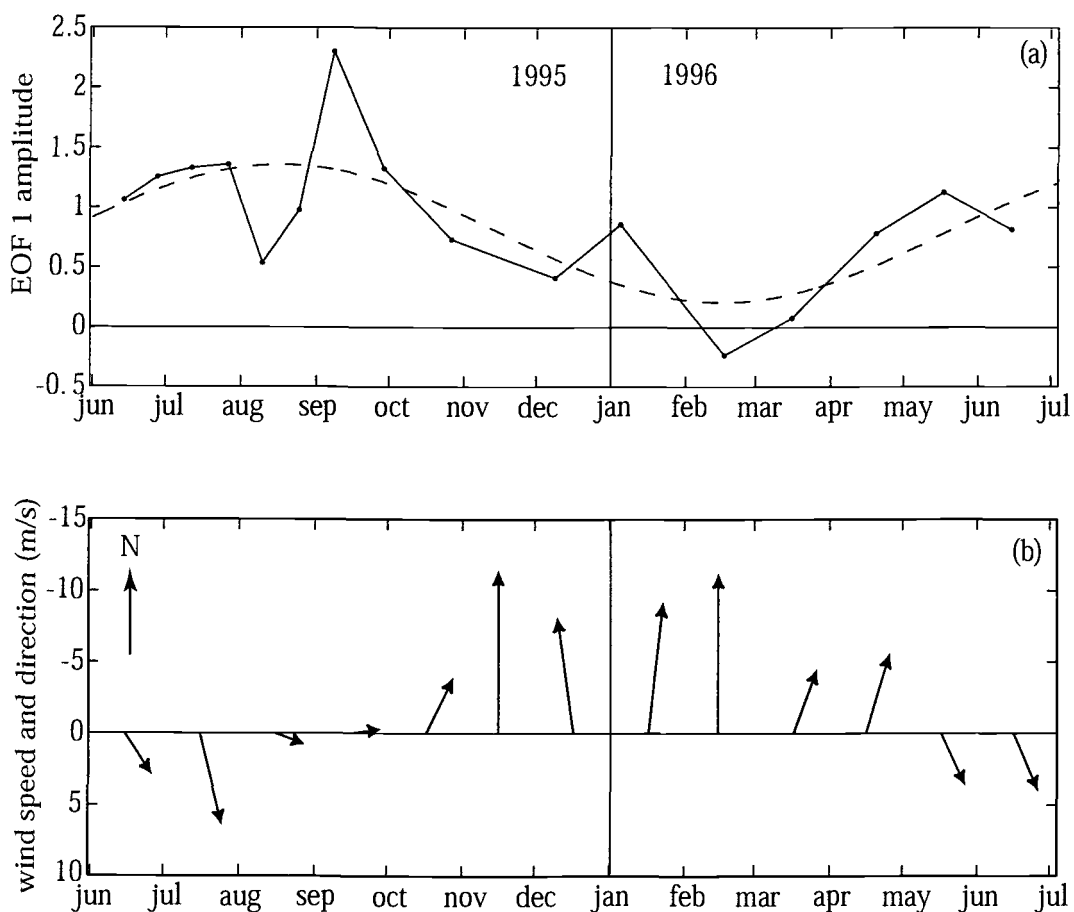


Figure 3.21 The dune mode EOF and monthly wind time series. **a)** The first year of the amplitude time series from the dune mode EOF (1995-96). A periodic, annual signal is plotted with the EOF time series to show the seasonal behavior of the dune mode. **b)** The monthly averaged wind speed and direction. Note the correlation between the seasonal dune mode amplitude and the wind time series. The erosion and disappearance of the dunes corresponds with the onset of the strong, southerly winds associated with winter.

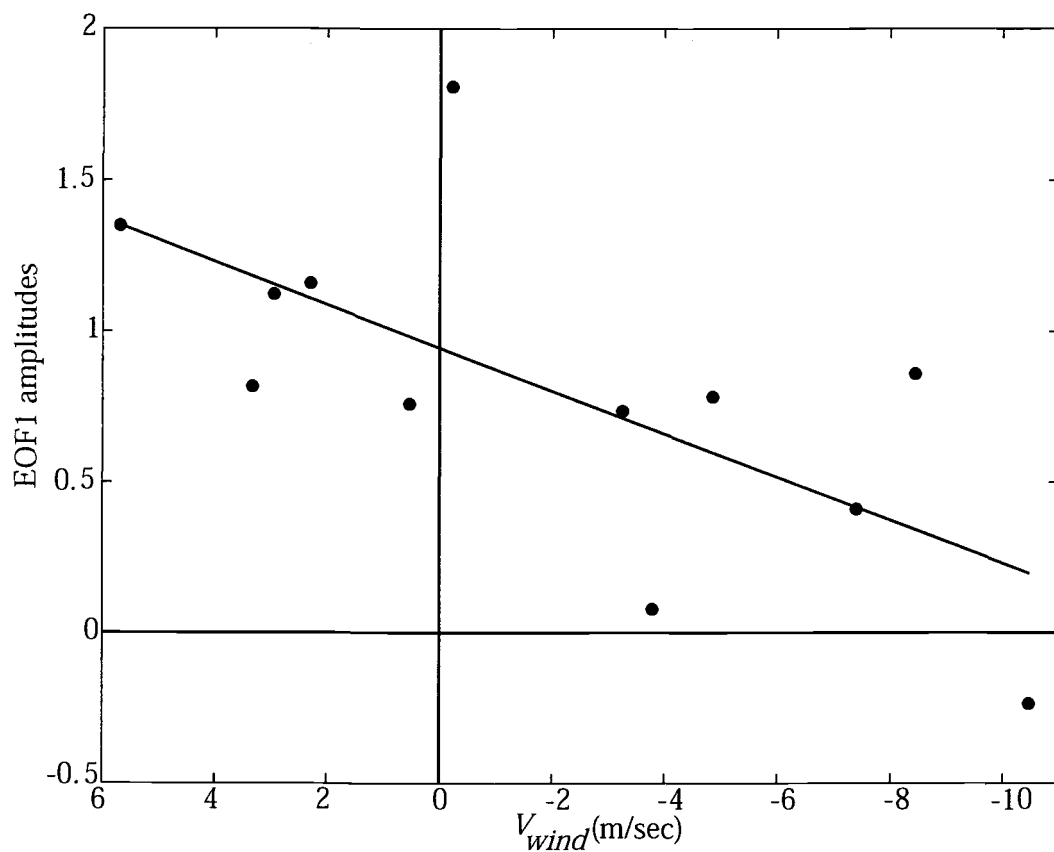


Figure 3.22 The monthly mean alongshore wind velocity v_{wind} plotted against the dune mode EOF amplitudes from the 1995-96 survey record showing the correlation between strong northwest summer winds and the growth of the backshore dune field.

alongshore wind velocity (v_{wind}) verses dune mode amplitudes from the 1995-96 survey year. The correlation between v_{wind} and the dune mode amplitudes ($\rho = 0.45$ with $\rho_{crit} = 0.36$ at 95% confidence level) relates the emergence of the backshore dune field to the northwest winds characteristic of the summer months. Probably more important in the building of the dune field is the lack of swash interaction on the upper beach. Without strong southern winds, setup is decreased as well as the lack of extreme runup from the larger waves characteristic of winter conditions. At the same time, precipitation levels fall dramatically. This allows the upper beach sediments to sufficiently dry and enables aeolian transport to dominate the sediment fluxes along the seacliff without the erosive nature of high energy swash and rain saturated conditions.

The second EOF mode describes a pattern related to the variance associated with the rest of the beach. This mode also shows little alongshore structure. The alongshore mean of the spatial pattern reveals a cross-shore profile response corresponding to the beach surface seaward of the region dominated by the dune mode (Figure 3.20b). Similar to the first mode, the amplitude time series of this beach mode reveals an annual pattern. During the summer and early fall of the first year of the amplitude time series, the positive values of the spatial pattern contribute to the beach variance. This is followed by winter months, where the amplitude time series switches sign and therefore the spatial pattern of the second mode becomes largely negative, stripping sediments from the beach. The alongshore uniform structure of both of the modes produced by the EOF analysis

suggest cross-shore sediment fluxes dominate the patterns of variability along Agate Beach on a seasonal cycle.

Estimates of net alongshore and cross-shore sediment fluxes, Q_{xy} , can be made based on calculation of time variations of the total sediment volume in the survey region. The volume contained within the box (Figure 3.23) is calculated as:

$$V_b(t) = \sum_i \sum_j z(t, x_i, y_j) \Delta x \Delta y \quad (15)$$

where $\Delta x = 10$ m, $\Delta y = 20$ m and only grid nodes that contain no missing data are used. The mean volume is then removed to produce the $V_b(t)$ time series shown in Figure 3.24. The $V_b(t)$ time series is modeled after equation 2 using a least squares multiple linear regression. The fit to the data, V_{model} , is significant at the 95% confidence level with $R = 0.97$ and $R_{crit} = 0.14$.

The alongshore uniform structure of the EOF spatial patterns and periodic nature of their temporal signatures suggest they are strongly related to a nearly balanced seasonal cross-shore flux of sediment (Figure 3.20). Assuming the net cross-shore flux (Q_x) within a year is close to zero, we model the change in beach volume $V_b(t)$ as a periodic, annual cross-shore sediment flux (Q_x) superimposed upon an interannual alongshore sediment flux (Q_y) to the north. Q_x is decomposed into a periodic signal described by a cyclical component and $\phi_V = -0.27 \text{ yr}^{-1}$ with a net annual transport of zero. Furthermore, assuming that Yaquina Head acts as a barrier to alongshore sediment transport, forcing alongshore transport gradients to zero at the headland, the β_V term in equation 2 corresponds to the net rate of

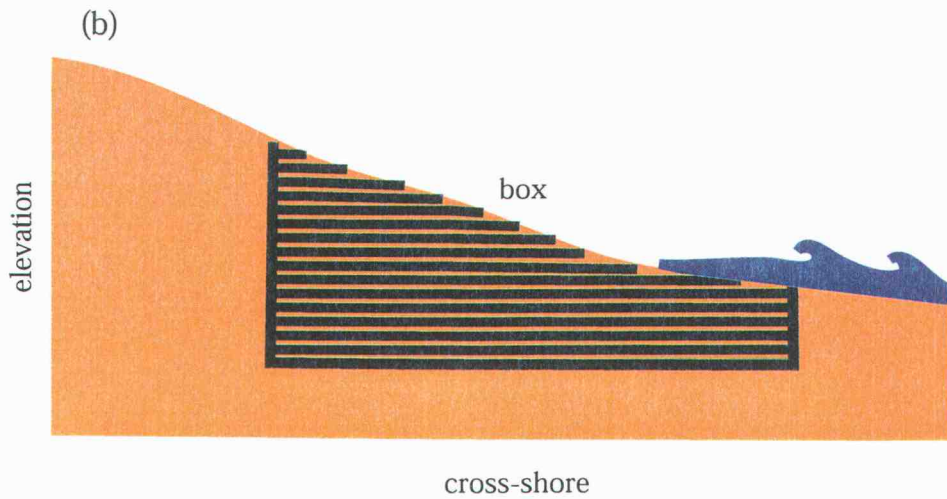
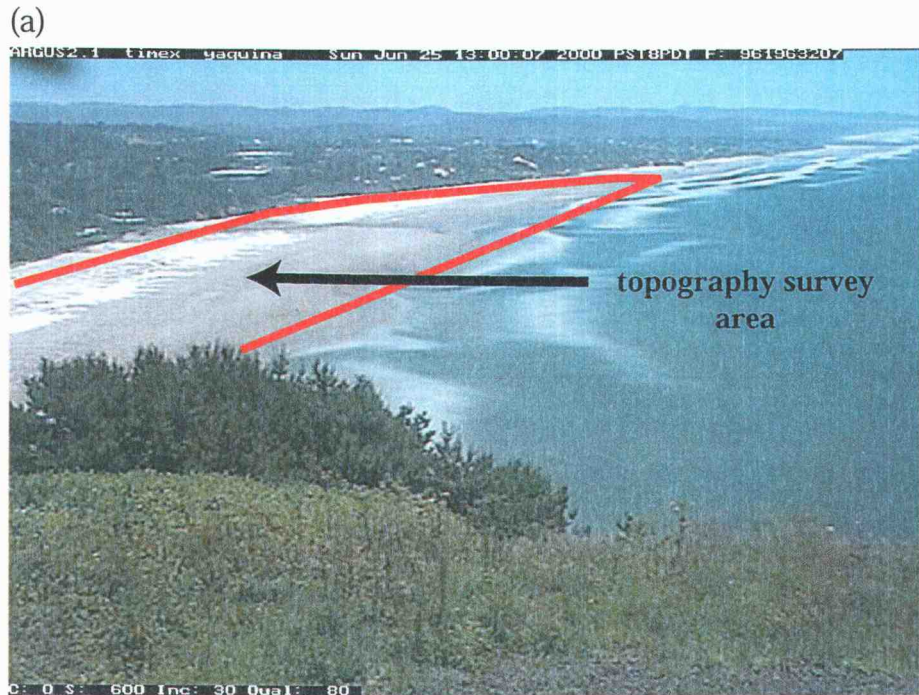


Figure 3.23 The survey area covered along Agate Beach. **a)** A time exposure image of Agate Beach collected by the Argus station on top of Yaquina Head. The box indicates the study area covered by the topographic surveys. **b)** A cross-shore schematic diagram of the volumetric sediment calculation from equation 15.

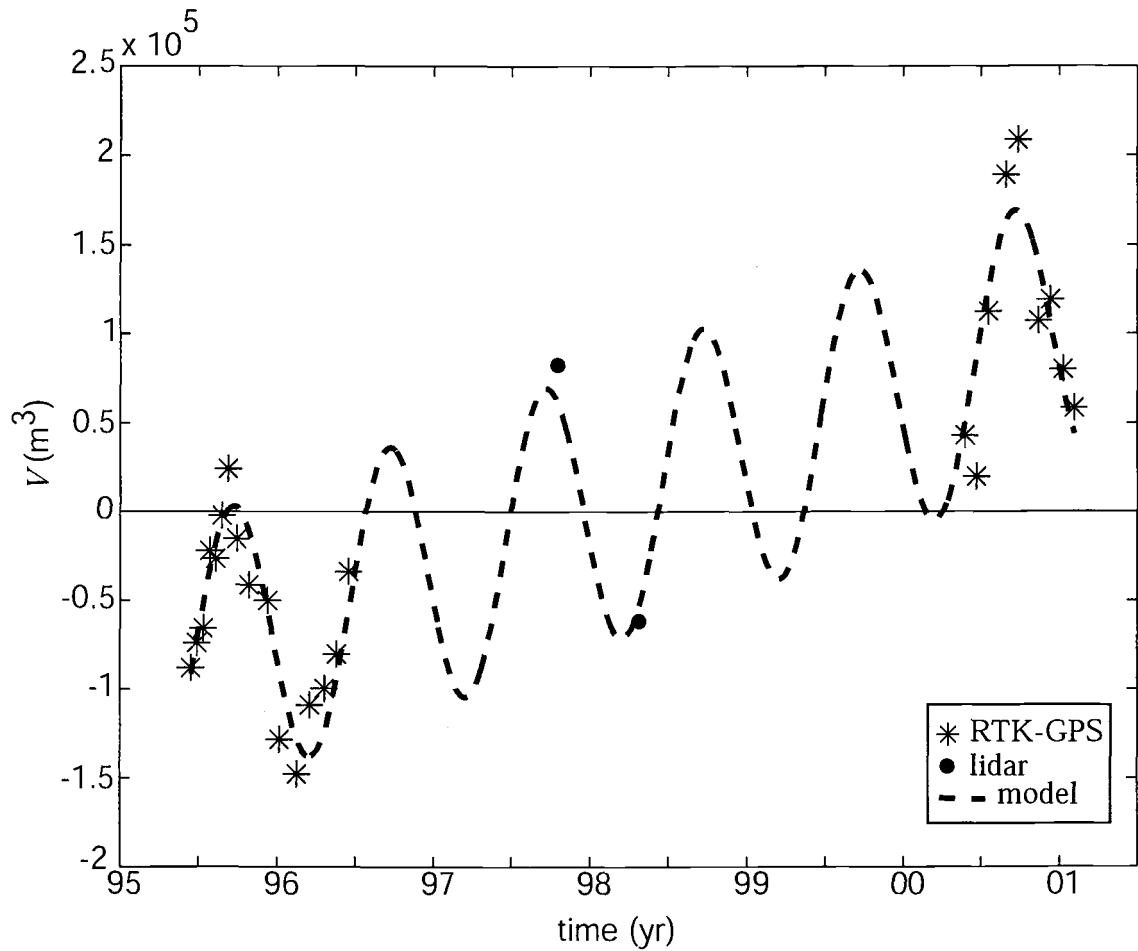


Figure 3.24 The demeaned beach volume time series, V_b , calculated from all of the topographic surveys. The dashed line represents a multiple least squares regression fit to beach volume estimates. The regression model is composed of a periodic seasonal cycle, an increasing linear trend, and an offset.

northward alongshore sediment transport $Q_y = 3.325 \times 10^4 \text{ m}^3/\text{yr}$. This is a net rate calculated over the survey record and a result of the accumulation of sand within the study area. A more exact description of Q_y would be defined from more frequent topographic sampling around episodic storm events that could be compared to estimates of Q_l from the wave conditions presented in section 3.2. A comparison between estimates of Q_y and Q_l is discussed in chapter 4.

3.5 Video Data Analysis

Spatial measurements from video images are made by transforming intensity values from pixel space (U and V) to the right hand local coordinate system common to the topographic survey data (x and y). The transformation from pixel space to real world coordinates is accomplished by standard photogrammetric techniques involving the geometric description of the camera position relative to the known positions of objects within the images (Holland et al., 1997). Each pixel in an oblique image (Figure 2.8) has an infinite number of corresponding real-world coordinates. However, by choosing the vertical coordinate to correspond to mean sea level, a unique map view, or rectification, can be computed (Figure 3.25a).

Three cross-shore transects are chosen from the straightened beach in W space (section 3.4.1). These coordinates (x' and y') are transformed into the local

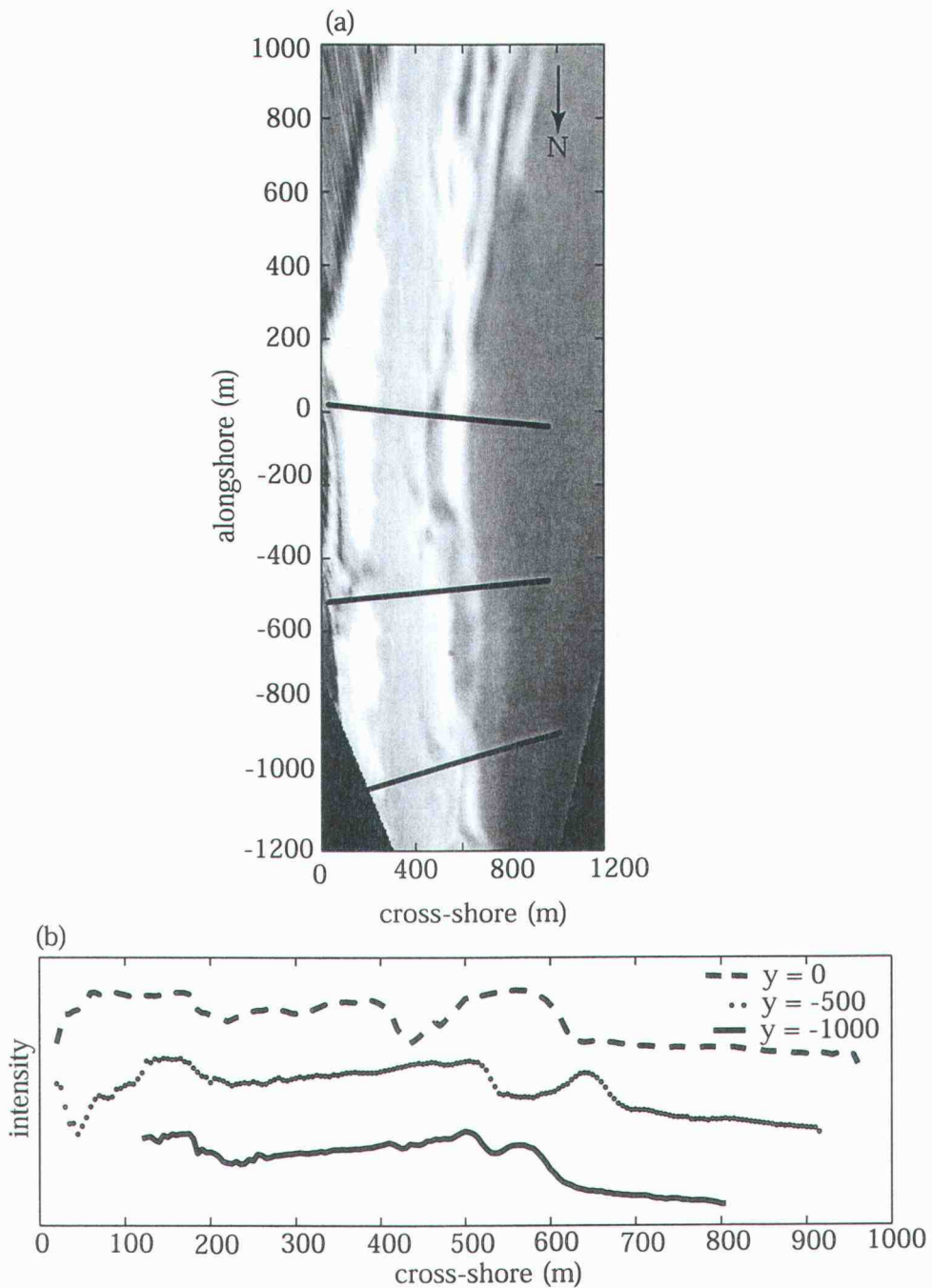


Figure 3.25 a) A rectified or plan view of the "daytimex" image from Figure 2.7 in local coordinates. Note the cross-shore transects have been corrected for the alongshore curvature of the beach. **b)** The pixel intensity profile corresponding to each of the cross-shore transects shown in (a). The peaks in intensity correspond to the cross-shore position of the sand bars.

coordinate system (x and y) by the inverse of the complex mapping described earlier (W space to Z space). From each daytimex image, intensity values corresponding to pixels nearest the x and y coordinates of each transect are interpolated onto those positions. This provides intensity estimates spaced at 5 m cross-shore intervals for 3 alongshore locations (Figure 3.25b).

Cross-shore intensity profiles from each daytimex image are used to build a space-time slice of image variability ($I(x,t)$) known as a timestack (Figure 3.26, Aargard and Holm, 1989, Holland and Holman, 1993). Time stack images resolve the time varying cross-shore position of the sandbars and shoreline. The timestacks are low-pass filtered in space to remove higher wavenumber variability using a Hanning window with a filter cutoff $\kappa_x < 0.0125 \text{ m}^{-1}$. Since the intensity range across each transect varies due to changes in insolation (e.g. cloud cover, seasons), each cross-shore profile is normalized to unit range.

Some bias may be introduced into our analysis due to the fact that wave breaking must occur over the sand bars in order for this optical method to resolve the cross-shore position of bathymetric highs. Thus measurement of the cross-shore position of the furthest offshore sand bars may be overly sensitive to surf zone width. However, because Agate Beach is continuously exposed to high wave energy, our technique appears to perform well with respect to locating the general cross-shore position of the outer sand bar.

The filtered and normalized timestacks provide a basis to analyze long-term sand bar behavior at Agate Beach. A measure of the time varying cross-shore

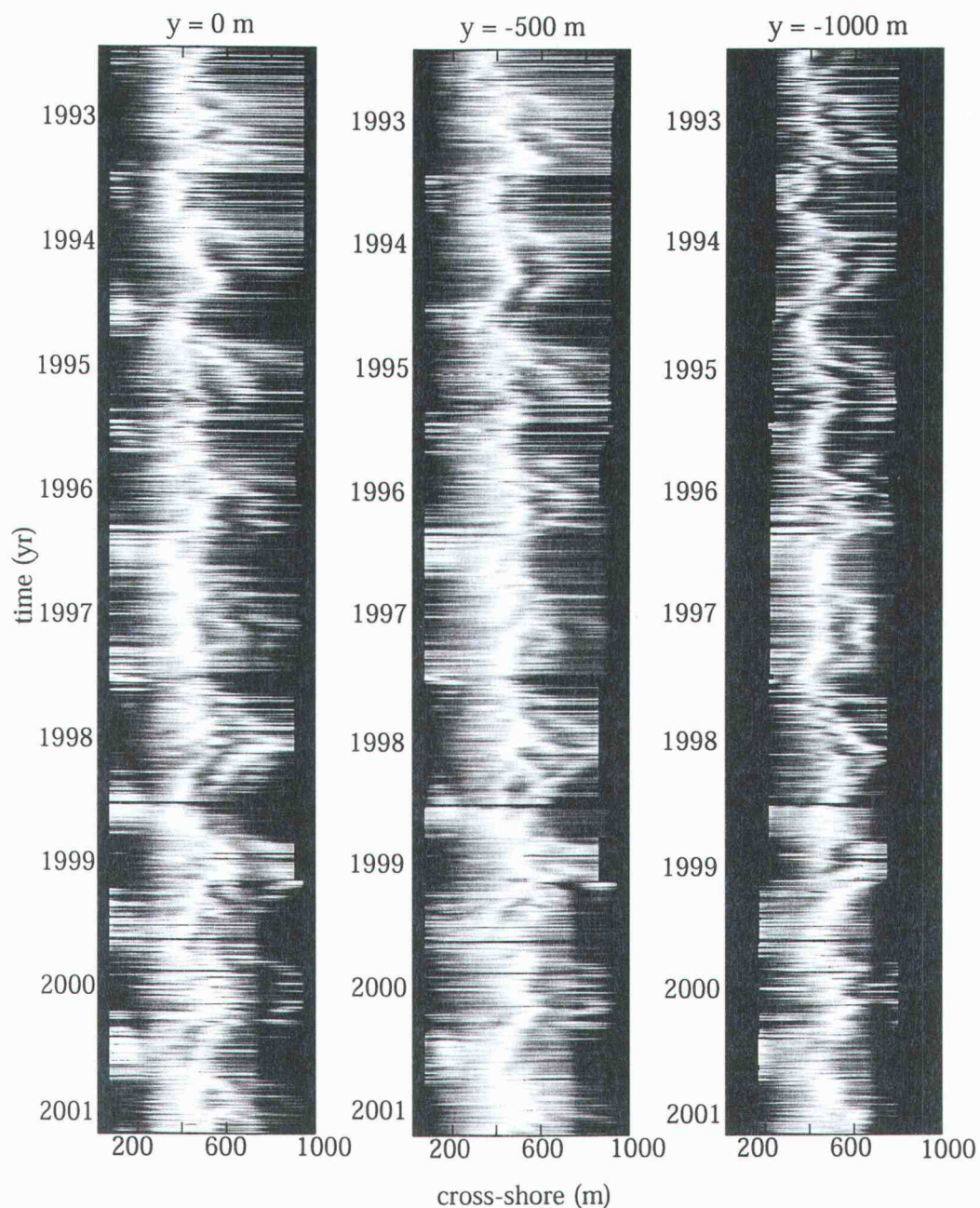


Figure 3.26 The normalized timestacks composed of "daytimex" images from the 3 cross-shore profiles shown in Figure 3.25. Note the periodic, seasonal nature of the bright bands of intensity related to the position of the offshore sand bars. Also important are the bright bands of intensity occurring in the backshore during the summer months. These areas are associated with the bright reflection of sunlight off the dry sand in the summer dune field.

position for the most seaward sandbar ($ob_{x,y}$) at each alongshore location is made with a second order Canny edge detection algorithm smoothing over one week intervals (Figure 3.27, Holland and Holman, 1996). An alongshore average of results from the three transects is used to estimate the time history of the general cross-shore location of the outer sandbar, OB_x , over the ~9 year video record (Figure 3.28).

To characterize the time varying cross-shore behavior of the outer bar, the OB_x time series is modeled after equation 2 using a multiple linear least squares regression. The model fit, OB_{xmod} , is significant at the 95% confidence level with $R^2 = 0.68$ and $R^2_{crit} = 0.54$ using Chelton's (1983) estimate for $N^* = 14$. OB_{xmod} is comprised of periodic intra-annual variability ($\omega = 2\pi/365 \text{ days}^{-1}$), an inter-annual long-term offshore trend and an offset. The periodic seasonal cycle has an amplitude $A_{OB} = 114.86 \text{ m}$ and phase $\phi_{OB} = 0.28 \text{ yr}^{-1}$ describing the offshore migration of the outer sand bar during winter and onshore return during summer conditions similar to the behavior of V_{model} from section 3.4.2. The long term, inter-annual seaward trend ($\beta_{OB} = 11.0 \text{ m/yr}$) in the cross-shore position of the outer sand bar described by OB_{xmod} also shows agreement with the long-term increase in beach volume described by V_{model} . Long-term growth in the volume of beach sands along Agate Beach corresponds with a seaward trend in the periodic annual migration of the outer sand bar.

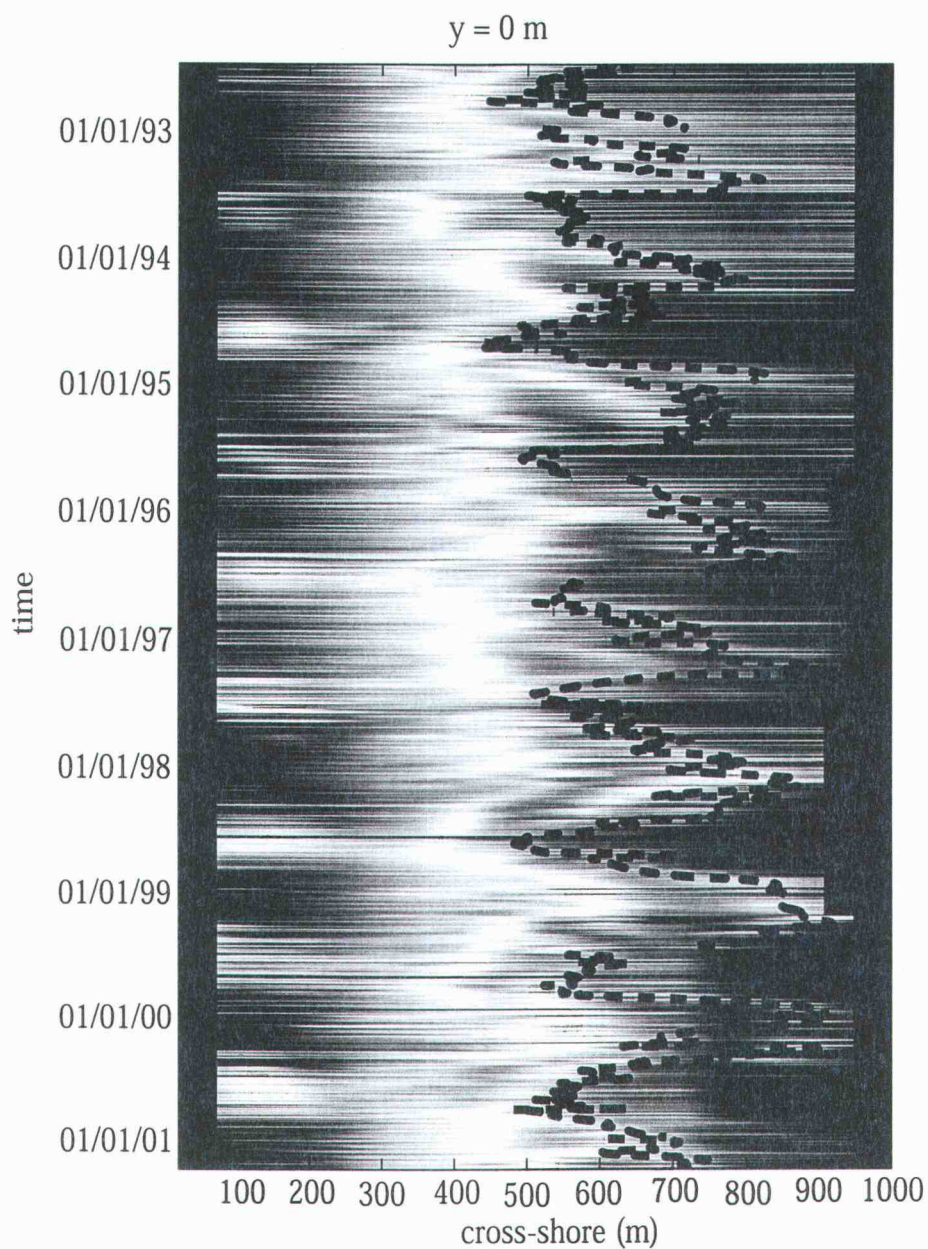


Figure 3.27 The "daytimex" timestack history of the cross-shore intensity profile at $y = 0 \text{ m}$. The cross-shore position of the seaward edge of the outer sandbar (ob_s), is acquired from a second order Canny edge detection algorithm.

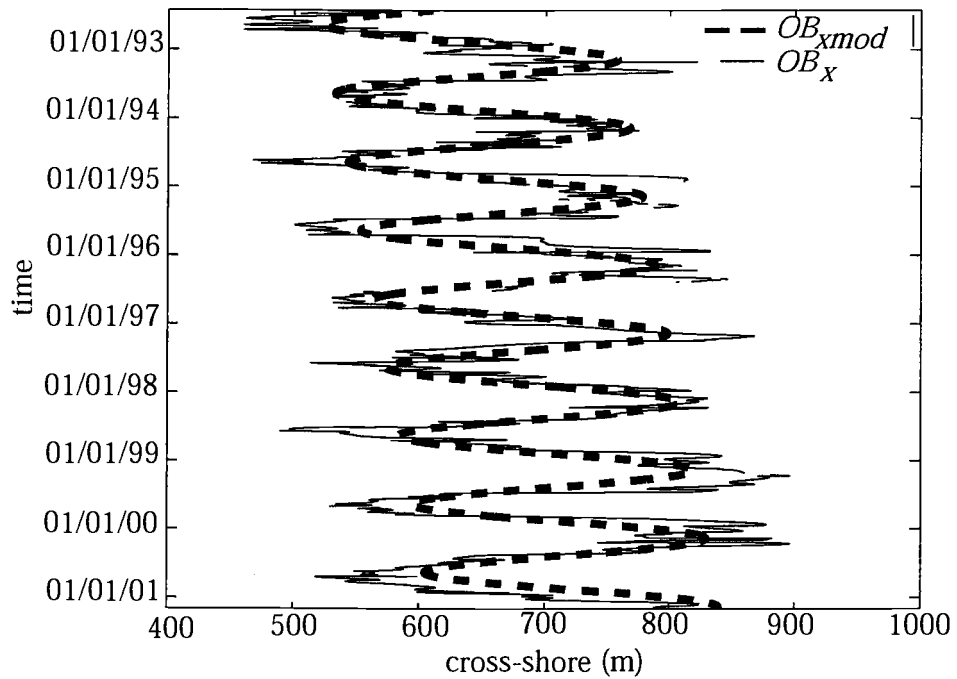


Figure 3.28 The alongshore averaged, cross-shore position of the outer sand bar, OB_x . The dashed line represents the least squares multiple linear regression fit to the OB_x time series after equation 2. The regression model, OB_{xmod} , is composed of a periodic, annual signal superimposed on a longer term offshore trend. This is consistent with the overall increase of sediment at Agate Beach described in section 3.4.

Chapter 4 DISCUSSION

The time series' of statistics describing the wave climate forcing and sediment response modeled in the previous sections are summarized in Table 4. The seasonal periodicity in both the forcing and sediment response are characterized as variance about a long-term, linear trend better defined as Large Scale Coastal Behavior, *LSCB*. The long-term increasing trend in H_s ($\beta_{H_s} = 6.7$ cm/yr) coupled with the low frequency reorientation in θ ($\beta_{\theta} = 3^\circ$ south/yr) combine to drive an accretionary regime at the northern end of the Newport littoral cell. Similarly, the *LSCB* observed in the β_V and β_{OBx} terms describing the long-term growth in sediment volume of the subaerial beach and the offshore migration of the outer sand bar support our hypothesis of net northward sediment transport and accumulation along Agate Beach. These results are also consistent with the expected sediment transport patterns associated with the 1997-98 El Niño and 1998-99 La Niña sequence. Except for V_b , an order of magnitude difference between the seasonal component of the modeled variability, A_x , and the long-term component, β_x , suggests seasonal variance dominates the signals on an annual basis.

The timing of the seasonal beach response to wave forcing is well resolved within the phase information obtained from the models. From Table 4 a yearly cycle generally proceeds as follows. In October H_s and T_p begin to increase, followed by a shift to a more southerly approach in θ . Similarly, the offshore

Table 4 Comparison of model coefficients for wave climate, beach sediment volume, and outer sand bar position. Confidence intervals are evaluated at the 95% level.

| Parameter | A_x | ϕ_x (yr ⁻¹) | β_x | β_{x0} |
|-----------|---|------------------------------|---|--|
| H_s | 0.94 m ± 0.06 | 0.36 ± 0.04 | 6.7 cm/yr ± 2.6 | 2.42 m ± 0.03 |
| T_p | 2.1 sec ± 0.1 | 0.35 ± 0.05 | 0.15 sec/yr ± 0.04 | 11.0 sec ± 0.06 |
| θ | 12.3° ± 2.0 | 0.30 ± 0.10 | 3° S/yr ± 0.8 | -3.5° ± 1.0 |
| V_b | 7.85x10 ⁴ m ³ ± 2.13x10 ⁴ | -0.27 ± 0.12 | 3.33x10 ⁴ m ³ /yr ± 4.6x10 ³ | -8.46x10 ⁴ m ³ ± 1.52x10 ⁴ |
| OB_x | 114.9 m ± 4.2 | 0.28 ± 0.04 | 11.0 m/yr ± 0.8 | 635.7 m ± 4.2 |

migration of OB_{xmod} lags the increase in H_s by roughly a month. Lastly, the decrease in the volume of sand on the beach lags the increase in H_s by ~45 days. Then, during spring conditions H_s begins to decrease, followed by the return of OB_{xmod} , and lastly, an increase in the volume of sand on the subaerial beach. This study quantifies the phase lag in the sediment response to the wave forcing. This is a crucial point in arguments between equilibrium and dynamic theories for cross-shore beach profile models. The observed phase lag of roughly 45 days between H_s

and V_b lies midway between the zero phase lag expected for equilibrium profile models and phase lag of $\pi/2$ expected for dynamic models.

Evaluating the performance of the predicted values of net alongshore transport from wave climate information ($\psi_{net} = 2.73 \times 10^8 \text{ m}^3$ north) with the measured values from topographic analysis ($\Delta V_{by} = 1.84 \times 10^5 \text{ m}^3$) reveals good agreement in the direction of transport to the north. However, the predicted magnitude of the transport is roughly 1500 times greater than our estimates from topographic data. The net increase in volume due to alongshore transport, ΔV_{by} , is calculated by subtracting the volume of the beach surface from the V_b time series when at its maximum in September 1995 from the maximum in September 2000. Since we attribute the long-term trend in the V_b time series to alongshore sediment flux, the net gain between maxima reveals the alongshore contribution of sediment to the study area.

The disagreement between the predicted and measured values of sediment transport may be related to the fact that Agate Beach is not a perfectly closed system. Leakage of sediment to the north around the headland during extreme wave events is likely. Our value for the predicted alongshore transport also neglects any aeolian influence during the summer season, which as we have shown is an important component of both the cross-shore and alongshore flux of sediment at Agate Beach. By including wind transport of sediment during the summer season, which would tend to remove sand to the south away from our study area,

better agreement in the predicted and measured alongshore sediment flux may be reached.

Discrepancies in our estimates of Q_l from offshore buoy statistics versus those used by Komar (1970) at the breaker zone may also contribute to slight errors in net transport calculations. Wave momentum flux (S_{xy}) must be conserved from deep water to the break point. Combining equations 7 and 8 yields

$$I_l = KcS_{xy} \quad (16)$$

where both K and S_{xy} remain constant. The ratio between estimates of alongshore sediment flux from deep water wave measurements (Q_{ldeep}) and Komar's (1970) estimates at the break point (Q_{lbp}) can then be revealed using equation 9.

$$\frac{Q_{ldeep}}{Q_{lbp}} = \frac{I_{ldeep}}{I_{lbp}} = \frac{c_{deep}}{c_{bp}} \quad (17)$$

From linear Airy wave theory

$$\frac{c_{deep}}{c_{bp}} = \frac{gT_{deep}/2\pi}{\sqrt{gh_{bp}}} \quad (18)$$

where T_{deep} is the deep water wave period and h_{bp} represents the depth of breaking. Using values of $T_{deep} = 10$ seconds and $h_{bp} = 4$ m typical of Agate Beach, the ratio between deep water and break point estimates of alongshore sediment flux (Q_{ldeep}/Q_{lbp}) is roughly 2.5. This value is far less than the $O(10^3)$ discrepancy observed in the measured and predicted sediment flux values.

Another source of error in the comparison between predicted and measured alongshore sediment flux may be due to a limited survey region. The long-term offshore migration of OB_x suggests sediment accretion over a much wider cross-shore region than the measured topographic survey area. Although, a portion of the long-term signal in OB_x may also be the result of the overall increase in H_s forcing the break point further offshore.

Analysis of the topographic survey data reveals the cross-shore structure of the time varying response of the beach surface to changes in wave and wind forcing. Alongshore parallel bands of increased variability around the 1m elevation contour coincide with distinct processes. The landward band is related to a seasonally wind generated dune mode that evolves during summer and early fall and is limited to the region above MHW. The seaward band of high variability is associated with a wave-driven mode affecting the remainder of the beach surface below MHW.

The analyses of wave forcing as a driving mechanism for $LSCB$ along Agate Beach is dependent on scale. The focus of this analysis is on larger scale changes spanning several years. By smoothing beach and sandbar variability at the appropriate temporal and spatial scales, good evidence exists for the directly forced beach response. At finer scales instabilities in the beach configuration may become important as feedback mechanisms for the overall beach evolution. For example, smaller scale rip channels and complex bar morphologies may contribute to the overall sediment transport offshore and alongshore by influencing the flow. These

types of smaller scale features contribute to the alongshore structure of the beach. In aggregate these features may bring the beach to a similar state as that predicted by the direct forcing from larger scale changes in wave climate. Still, for this study the long-term and seasonal behavior of the beach system at larger spatial scales appears to be directly forced by annual and lower frequency variability in the wave climate.

Chapter 5 SUMMARY AND CONCLUSIONS

Using buoy and anemometer data, as well as topographic surveys and video images, this study quantifies the forced response of a high energy, Pacific Northwest beach to variations in wave climate.

Significant wave heights, H_s , peak periods, T_p , and wave angles, θ , obtained from Oregon coastal buoys describe the incident wave field at Agate Beach.

Seasonal changes in amplitude ($A_{H_s} = 0.94 \text{ m} \pm 0.06$, $A_{T_p} = 2.1 \text{ sec} \pm 0.1$, $A_\phi = 12.3^\circ \pm 2.0$) provide much stronger variations in the forcing when compared to the long-term increase of H_s and T_p and reorientation of θ ($\beta_{H_s} = 6.7 \text{ cm/yr} \pm 2.6$, $\beta_{T_p} = 0.15 \text{ cm/yr} \pm 0.04$, $\beta_\theta = 3^\circ \text{ S/yr} \pm 1.0$). The long-term increase in incident wave energy is accompanied by a reorientation to a more southerly approach in wave angle. Assuming wave-driven currents dominate alongshore sediment fluxes and transport gradients go to zero at the headland, predictions of alongshore sediment transport from wave climate data estimate an accretionary volume transport of $\psi_{\text{net}} = 2.73 \times 10^8 \text{ m}^3$. The measured volumetric accretion within the survey area at Agate Beach is $\Delta V_{\text{by}} = 1.84 \times 10^5 \text{ m}^3$.

Quantitative analysis of 27 topographic surveys spanning 6 years resolves the annual and long-term sediment response of Agate Beach to variations in wave forcing. Alongside the seasonal loss of beach sands during winter and subsequent return of sediment during calmer summer months ($A_{\nu_b} = 7.85 \times 10^4 \text{ m}^3 \pm 2.13 \times 10^4$), a general long-term increase in beach volume is observed ($\beta_{\nu_b} = 3.33 \times 10^4 \text{ m}^3/\text{yr} \pm$

4.6×10^3). Unlike the wave climate variables, the magnitudes of seasonal and long-term sediment volume changes are very similar. Elevation change estimates over the record length are large with some regions of the beach exhibiting elevation gains up to 3 m. Consistent with the long-term growth in subaerial beach volume, ~9 years of video data show a steady long-term offshore migration rate of the outer sand bar ($\beta_{OBx} = 11.0 \text{ m/yr} \pm 0.8$). This long-term offshore migration is coupled with seasonal fluctuations in cross-shore position ($A_{OBx} = 114.9 \text{ m} \pm 4.2$) as a response to variations in wave climate.

Besides describing the response of the beach in terms of sediment volume and cross-shore position of the outer bar, this analysis also decomposes the cross-shore structure of the time varying beach surface using 2 eigen modes. The first mode is characterized by the seasonal growth of a dune field explaining 34% of the variance in the data. This mode of variability is limited to elevations above MHW. The dune mode is wind forced and correlated to summer winds and lack of precipitation and swash above MHW. The second mode describes the seasonal variability in the beach surface related to wave driven processes. This mode explains 21% of the variance and describes the beach surface changes below the MHW. The cross-over between these modes of variance is observed around MHW elevation at $z = 1.076 \text{ m}$. Landward and seaward of MHW, the beach responds to forcing in two alongshore bands of increased variability.

Although the regression models developed in this analysis quantitatively describe the seasonal and long-term variability in both the forcing and response of

the Agate Beach system, an improved description of the *LSCB* can be obtained by continued topographic surveys and collection of video, buoy and anemometer data. The long-term increasing trends identified in this analysis may actually represent portions of lower frequency variability that is not resolved within the current record length. Perhaps these trends in wave climate forcing are related to long-term oscillations in regional oceanic conditions as suggested by Allan and Komar (2000).

REFERENCES

- Aagard, T., and J. Holm, 1989, Digitization of Wave Runup Using Video Records. *J. Coastal Res.*, 5, 547-551.
- Allan, J. and P.D. Komar, 2000, Are ocean wave heights increasing in the eastern north pacific? *EOS Trans., Amer. Geophys. Union*, 81(47), 561-567.
- Aubrey, D.G., 1979, Seasonal patterns of onshore/ offshore sediment movement. *J. Geophys. Res.*, 84, 6347-6354.
- Aubrey, D.G., 1983, Beach changes on coasts with different wave climates. *Sandy Beaches as Ecosystems*: Dr. W. Junk Publishers, The Hague, 63-86.
- Bagnold, R.A., 1984, *The Physics of Blown Sand and Desert Dunes*. Chapman and Hall, London New York, 256 pp.
- Birkemeir, W.A., 1984, Time scales of nearshore profile changes. *Proceedings Coastal Engineering '84*, New York, ASCE, 1507-1521.
- Birkemeier, W.A., H.C. Miller, S.D. Wilhelm, A.E. DeWall, and C.S. Gorbics, 1985, *A User's Guide to CERC's Field Research Facility*. Coastal Engineering Research Center, U.S. Dept. of the Army, Waterways Experiment Station, Corps of Engineers, Instruction Report CERC-85-1.
- Bowen, A.J., 1969, The generation of longshore currents on a plane beach. *J. Marine Res.*, 27, 206-215.
- Chelton, D.B., 1983, Effects of sampling errors in statistical estimation. *Deep-Sea Res.*, 30, 1083-1103.
- Dail, H.J., M.A. Merrifield and M. Bevis, 2000, Steep beach morphology changes due to energetic wave forcing. *Mar. Geol.*, 162, 443-458.
- Davis, R.E., 1976, Predictability of sea surface temperature and sea level pressure anomalies over the North Pacific Ocean. *J. Phys. Oceanography*, 6, 249-266.
- De Vriend, H.J., 1997, Prediction of aggregated scale coastal evolution. *Proceedings Coastal Dynamics '97*, New York, ASCE, 644-653.

- Gallagher, E.L., S. Elgar, and R.T. Guza, 1998, Observations of sand bar evolution on a natural beach. *J. Geophys. Res.*, 103, 3203-3215.
- Guza, R.T. and E.B. Thornton, 1981, Wave setup on a natural beach. *J. Geophys. Res.*, 86(C5), 4133-4137.
- Holland, K.T. and R.A. Holman, 1993, The statistical distribution of swash maxima on natural beaches. *J. Geophys. Res.*, 98, 10271-10278.
- Holland, K.T. and R.A. Holman, 1996, Field observations of beach cusps and swash motions. *Mar. Geol.*, 134, 77-93.
- Holland, K.T., R.A. Holman, T.C. Lippman, J. Stanley, and N.G. Plant, 1997, Practical use of video imagery in nearshore oceanographic field studies. *IEEE J. Oceanic Eng.*, 22(1), 81-92.
- Holman, R.A. and T.C. Lippman, 1987, Remote sensing of nearshore bar systems - making morphology visible. *Coastal Sediments*, 87, 929-944.
- Holman, R.A. and T.C. Lippman, 1998, Workshop summary report of the large scale working group. *Nearshore Processes Workshop*, St. Petersburg, FL.
- Komar, P.D. and D.L. Inman, 1970, Longshore sand transport on beaches. *J. Geophys. Res.*, 75, 5914-5927.
- Komar, P.D. and J. Oltman-Shay, 1990, Nearshore Currents. *Handbook on coastal and Ocean Eng.*, Gulf Publishing Co., Houston, TX, 2(10), 651-680.
- Komar, P.D., 1986, The 1982-83 El Niño and erosion on the coast of Oregon. *Shore and Beach*, 54, 3-12.
- Komar, P.D., 1997, *The Pacific Northwest Coast: Living With the Shores of Oregon and Washington*. Duke University Press, U.S., 195 pp.
- Komar, P.D., 1998a, The 1997-98 El Niño and erosion on the Oregon coast. *Shore and Beach*, 66(3), 33-41.
- Komar, P.D., 1998b, *Beach Processes and Sedimentation*. Prentice-Hall Inc., New Jersey, 543.
- Konicki, K.M. and R.A. Holman, 2000, The statistics and kinematics of transverse sand bars on an open coast. *Mar. Geol.*, 169, 69-101.

- Longuet-Higgins, M.S., 1952, On the statistical distribution of the height of sea waves. *J. Marine Res.*, 11, 245-266.
- Longuet-Higgins, M.S., 1970, Longshore currents generated by obliquely incident waves. *J. Geophys. Res.*, 75, 6778-6789.
- Morton, R.A., M.P., Leach, J.G., Paine and M.A. Cardoza, 1993, Monitoring beach changes using GPS surveying techniques. *J. Coastal Res.*, 9, 702-720.
- O'Neil, P.V., 1995, *Advanced Engineering Mathematics*. PWS Publishing Co., Boston, MA, 1105 pp.
- Plant, N.G. and R.A. Holman, in review, The use of GPS observations of intertidal beach variability to describe the relative importance of cross-shore and alongshore sediment transport mechanisms. submitted *J. Geophys. Res.*, 32 pp.
- Plant, N.G., R.A. Holman, M.H. Freilich, and W.A. Birkemeier, 1999, A simple model for interannual sandbar behavior. *J. Geophys. Res.*, 104(C7), 15755-15776.
- Ruessink, B.G. and J.H.J Terwindt, 2000, The behavior of nearshore bars on the time scale of years: a conceptual model. *Mar. Geol.*, 163, 289-302.
- Ruggiero, P., 1997, Wave runup on high energy dissipative beaches and the prediction of coastal erosion. Corvallis, Oregon: Oregon State University, Ph.D. thesis, 145 pp.
- Sallenger, A.H., R.A. Holman, and W.A. Birkemeier, 1985, Storm induced response of a nearshore bar system. *Mar. Geol.*, 64, 237-257.
- Sallenger, A.H., et al., 1999, Airborne laser study quantifies El Nino-induced coastal change. *EOS*, American Geophysical Union, 80: 92-93.
- Sallenger, A.H., W. Krabill, et al., in review, Evaluation of airborne scanning lidar for coastal change applications. submitted *J. Coastal Res.*, 16 pp.
- Schlx, M.G. and D.B. Chelton, 1992, Frequency domain diagnostics for linear smoothers. *J. Amer. Statistical Assoc.*, 87(240), 1070-1081.
- Stive, M.J.F., H.J. De Vriend, P.J. Cowell and A.W. Niederoda, 1995, Behavior oriented models of shoreface evolution. *Proceedings Coastal Dynamics '95*, New York, ASCE, 998-1005.

- Thornton, E.B., 1970, Variations of longshore current across the surf zone. *Proceedings of the 12th Coastal Engineering Conference, Amer. Soc. Civil Engrs.*, 291-308.
- Thornton, E.B. and R.T. Guza, 1986, Surf zone longshore currents and random waves: field data and models. *J. Phys. Oceanography*, 16, 1165-1178.
- Van Enckevort, I.M.J, 2001, Daily to yearly nearshore bar behavior. Utrecht University, Ph.D. thesis, 171pp.
- Wijnberg, K.M., and J.H.J. Terwindt, 1995, Extracting decadal morphological behavior from high resolution, long-term bathymetric surveys along the Holland coast using eigenfunction analysis. *Mar. Geol.*, 126, 301-330.
- Winant, C.D., D.L. Inman and C.E. Nordstrom, 1975, Description of seasonal beach changes using empirical eigenfunctions. *J. Geophys. Res.*, 80(15), 1979-1986.
- Wright, L.D. and A.D. Short, 1983, Morphodynamics of beaches and surf zones in Australia. *Handbook of Coastal Proc. And Erosion*. CRC Press, Boca Raton, FL, 35-64.